Universiteit Utrecht

UMC Utrecht

Faculty of Science

A numerical study on the sub- and ultraharmonic response of an oscillating microbubble in a rigid tube

Bachelor Thesis

Roos Meijer

Physics and astronomy

Supervisors:

Dr. Joost de Graaf
Institute for Theoretical Physics

Dr. Mario Ries
Imaging Division UMCU

03-07-2020

Abstract

Recently, various research within ultrasound is done on the applications of sub- and ultraharmonics responses from microbubbles, for the use in therapeutic high-intensity focused ultrasound (HIFU) and diagnostic ultrasound. Even tough some results are promising, often these experiments are done in *in vitro* experiments that are not comparable to *in vivo* situations, or the *in vivo* data is compared to models that do not account for damping due to the capillary wall surrounding the oscillating microbubble (e.g the solution of the Rayleigh-Plesset equation in free water). In this thesis we investigated a model that includes the influence of a restricted oscillation in a capillary tube, and compared qualitatively the sub- and ultraharmonic response from this model to the solution of the Rayleigh-Plesset equation in free-water. In addition to this, we investigated the impact of the viscosity on the free-water oscillation of the microbubbles and the sub- and ultraharmonic responses. We found that that for high viscosities the sub- and ultraharmonic responses get highly dampened and eventually disappear. The treshold for full suppresion was thereby predicted by theory for a viscosity of 1.3 mPas for ultraharmonics and above 2.2 mPas for the subharmonic. Also, we found that the responses shift to smaller microbubble sizes when a tube is added around the oscillating microbubble.

Contents

1 Introduction

Ultrasound is a non-invasive imaging technique that has many clinical uses in medicine. Ultrasound can visualize large arteries, organs and fetuses in the body with sound waves at high frequencies (from 1 MHz to 10 MHz). The transmitted beam is reflected and scattered by tissue and local impedance changes, which reveal anatomical as well as pathological information. The power spectra of these reflected waves get analysed and a visualization can be made of these tissues [1]. Although the differences between hard and soft tissue are well distinguished, the transition between different types of soft tissues are less well defined. The resolution of ultrasound images can be enhanced with microbubbles that are used as an intravascular contrast agent. When a microbubble, filled with gas, is insonicated with an ultrasound beam, it starts to oscillate: it becomes a frequency dependent scatterer of the exciting sound wave. Depending on the parameters of the transmitted beam and the microbubble, this oscillation is non-linear. Due to this, the microbubble does not only scatter sound with the principal frequency with which the system is insonicated, but also scatters higher harmonics: integer multiples of the principal frequency[2]. Noteworthy is hereby, that sound at higher pressures displays a non-linear propagation leading to harmonic spectral components in soft tissue, but in a less prominent way.

In the past couple of decades, there have been several developments in making ultrasound a therapeutic technique. These came together with the development of coated microbubbles that have a type of shell around them that makes them last longer in the body and stabilizes their oscillation. In diagnostic imaging, these contrast agents increase the resolution between flowing blood and surrounding tissue once they are injected into the body [3].
One of those therapeutic usages of ultrasound is called High-intensity focused ultrasound (HIFU). Although the frequencies are lower when using HIFU, the energy levels are much higher. The intensity of the beam is increased by focusing it all onto one spot. The high temperatures that occur due to the elevated local acoustic absorption can kill cells in that area, even with a short exposure time [4]. Contrast agents can help increase the accuracy of the location that needs to be insonicated with HIFU.
Another therapeutic application for HIFU and contrast agents is in the brain. The brain is separated from the rest of the body by the blood-brain barrier (BBB). This BBB keeps more than 98% of therapeutic drugs (large and small molecules) from entering the brain [5]. While this protective layer is essential for the functioning of the central nervous system, it complicates therapy of pathologies originating in the brain. It was found that when HIFU is focused on some part of the brain, and contrast agents are injected, the BBB can become disrupted by the oscillating microbubbles and larger molecules can go through. The parameters that are used are very important in this process, because surrounding tissue can become damaged due to this BBB disruption [6]. At high pressures, depending on the initial microbubble radius, the microbubble can transition to a violent oscillation stage known as 'inertial cavitation'. Either the microbubble only survives the oscillations for a couple of cycles, after which it breaks, or it has a strong collapse phase in its oscillation cycle that can result in light emission and/or chemical reactions [7]. The transition from stable to inertial cavitation happens at a certain pressure threshold that depends on the parameters of the system and the microbubble. The violent oscillation of inertial cavitation, with the phenom-

ena that follow, can cause damage to neighbouring tissue. Determining what the correct parameters are is very difficult, and can differ per location in the brain and per person.

Sub- and ultraharmonics might be the answer to this problem. Subharmonic frequencies are halve the principal frequency and are a phenomenon of the non-linear oscillation of a microbubble. Ultraharmonics are higher harmonics of the subharmonic.
It has been shown that the difference between the subharmonic response of contrast agents and tissue is larger than that of the first harmonic. This means that the resolution of images can be improved if processed with subharmonics [8]. It also suggests that we can see in the signal from the scattered wave whether microbubble are still present or have been fragmented due to inertial cavitation. This could increase the safety of using HIFU in the brain. Already, research has been done on the effects of specific acoustic parameters and bubble distribution on the subharmonic response of the contrast agent Sonovue® for abdonimal imaging [9]. In this research they determined the ideal acoustic characteristics to maximalize the subharmonic response of Sonovue. Although this research gives a good insight on the ideal setup for subharmonic detection, it does not take into account the change in bubble dynamics when a contrast agent is insonicated *in vivo*[1].

In recent experiments inside the brain of a mouse, no subharmonics or ultraharmonics were found inside the scattered signal, despite evidence of BBB disruption when insonication with a pressure of 400 kPa. For higher pressures than 600 kPa some subharmonics and ultraharmonics were found, but there was also tissue damage in the vicinity of the opening site and over the entire spectrum the noise floor came up[2] [10]. This might suggest that sub- and ultraharmonics are phenomena that can be related to inertial cavitation. It is thus important that we understand the difference between *in vitro*[3] and *in vivo* set ups, and how the scattering spectrum of the microbubbles is modified in the respective situations, in order to distinguish reliably between inertial and stable cavitation.

The established theoretical model for the dynamics of the oscillation of a bubble is the Rayleigh-Plesset equation. This equation considers the oscillation of a bubble in an infinite fluid domain. However, for microbubbles oscillating inside capillaries this model has to be extended to include the interaction with the vessel wall. This extension was done in the paper by Qamar et al. [11]. In this thesis we will test this model and compute the sub- and ultraharmonic response. Then, we will compare it to the sub- and ultraharmonic response simulated by the Rayleigh-Plesset equation.
We will also look into the influence of the viscosity on the change in sub- and ultraharmonic response of microbubbles simulated with the Rayleigh-Plesset equation. This is done because blood has a higher viscosity than fluids such as water, which are often used in *in vitro* experiments. To conclude, we will be looking at the influence of two independent parameters: the influence of the viscosity and the additional hydrodynamic damping introduced by the vicinity of a vascular wall.

[1] Taking place inside the body of a living organism

[2] The acoustic noise in the spectral density of the scattered wave can be related to certain inertial cavitation phenomena [7].

[3] Taking place outside the body of a living organism

In chapter 2 of this thesis we will go over the theory needed to understand the physics of the models that will be used. First we briefly go over the non-Newtonian characteristics of blood. Subsequently, we will go into the fundamental equations of fluid dynamics: the Navier-Stokes equations and also some more detailed physics needed. Chapter 3 is dedicated to the theoretical derivation of the extended model by Qamar et. al. [11], and key point for the simulation of this model. Chapter 4 gives the results and discussion of our model, where we will discuss the influence of the viscosity and wall boundary in separate sections. Lastly, in chapter 5 we draw conclusions to the questions raised in the introduction.

2 Theory

In this section we will go over the theory needed to understand the method described in section 3. In section 2.1 we go over some non-Newtonian phenomena of blood and why it is a difficult fluid to work with. In section 2.2 we derive the Navier-Stokes equation for a better understanding of the theories in the sections that follow. In section 2.3 we look at the Rayleigh-Plesset equation, which is the equation that is mostly used today to simulate the oscillation of a microbubble. A goal for our model is that it is similar in form and usage, and thus can be easily compared to the Rayleigh-Plesset equation.
In section 2.5 we go over the basics of fluid theory that are required to describe laminar flows inside tubes. Our own model will try to incorporate this theory into the Rayleigh-Plesset equation. At last, in section 2.4 the shell model is described that is used during our simulation.

2.1 Blood as a Non-newtonian fluid

Fluids are classified as *Newtonian* or *non-Newtonian*. A fluid is called Newtonian when the shear stress of the fluid is directly proportional to the strain rate. When this is not the case a fluid is referred to as non-Newtonian. Newtonian fluids are further discussed in section 2.2. The emphasis of this section lies on non-Newtonian fluids, in particular the non-Newtonian fluid blood.

The shear stresses of a fluid develop due to viscous flow. Often, for non-Newtonian fluids the term *apparent viscosity* η is used to describe the viscosity. The difference between the Newtonian viscosity μ and apparent viscosity η is that μ is constant (ignoring temperature effects) and η is dependent of the shear rate. For some non-Newtonian fluids this relation can be experimentally determined, but unfortunately for blood as a complex fluid-solid mixture this is much more complicated.
The most important parts of blood are the red blood cells ($\sim$41%) and the blood plasma ($\sim$45%), whereby these percentages can change with conditions and location. The remaining 4% are other types of cells in the blood such as white blood cells an platelets. The viscosity of blood depends on the viscosity of blood plasma, the proteins present in the blood plasma, the ratio of blood plasma to cells (i.e. hematocrit), the temperature, the shear rate and the diameter of the vessel [12]. The later means that the viscosity of blood in major arteries is different from that in small capillaries. This effect is called the *Fahraeus-Lindqvist effect*. For vessels between $15\,\mu\text{m} < D < 500\,\mu\text{m}$ in diameter the viscosity decreases with decreasing vessel diameter. For vessels smaller than $15\,\mu$m the viscosity increases again.

In summary, the resulting effects of the change in viscosity due to vessel size is an important phenomenon for this research. Depending on the vessel diameter the viscosity can change, which can change the dynamics of the oscillating bubble. As a consequence, a realistic simulation of the *in vivo* situation becomes a lot more complicated this way. Since it is important, as mentioned in the introduction, we will look at the dependence of a changing viscosity on dynamics of an oscillating microbubble.

2.2 Navier-Stokes equations

Depending on the specific research question, there are two fundamental approaches to describe motion of fluid [13]:

1. look at a larger region of space and see how the fluid behaves there.
2. study the motion of an individual fluid particle or a group of particles.

The approach we will be using is the individual fluid particle approach. In this approach we can work directly with known physical interactions on the individual particle. And if we solve the trajectory of a particle on a particular streamline[4] we can find the growth and collapse of the microbubble-fluid interface. A downside of this approach though, is that the mathematics can become complicated and along the way some assumptions and approximations will have to be made to solve the problem. This individual particle approach will lead us to a set of partial differential equations that describe the flow of incompressible fluids: the *Navier-Stokes equations*. Because of the importance of the Navier-stokes equations in fluid dynamics and to the understanding of the method used in this research, we will briefly introduce the Navier-Stokes equations in this section. We will treat these equations in Cartesian coordinates. Although Cartesian coordinates are often not ideal in the type of problems we are interested in, they are however more convenient for explaining the derivation of these equations.

For the derivation of the Navier-Stokes equation we largely follow the explanation of section 6.2 from the book *Introduction to Fluid Mechanics* by Nakayama and Boucher [14] and the derivation of section 2.4 from the book *Viscous Fluid Flow* by White [15].

Consider a small rectangular fluid element with dimension $dx \times dy \times b$ and apply Newton's second law on it. The dimensions of the rectangular element are as seen in figure 2.1, where we are only looking at a two dimensional problem in Cartesian coordinates. This choice is motivated by the symmetry of the problem, which allows subsequently to reduce the problem from three spatial dimensions to two or one dimensions. For now, the third dimension can be taken into account by the thickness of this element as b, and the density of the fluid as ρ. In this situation we get the following equations for the x and y direction:

$$\begin{aligned} \rho\, b\, dx\, dy\, \frac{du}{dt} &= dF_x \\ \rho\, b\, dx\, dy\, \frac{dv}{dt} &= dF_y\,, \end{aligned} \tag{2.1}$$

with u the velocity in the x-direction and v the velocity in the y-direction. The left-hand side of the equations represents the inertia force of the fluid element and the right-hand side of the equations represents the forces that are exerted on the fluid element. In Newton's second law (equation (2.1)) we know that the inertial force is the product of the mass of the fluid element and the acceleration. The change in velocity here does not only depend on the

[4] A streamline is a curve formed by the velocity vectors of each fluid particle at a certain timestep [14].

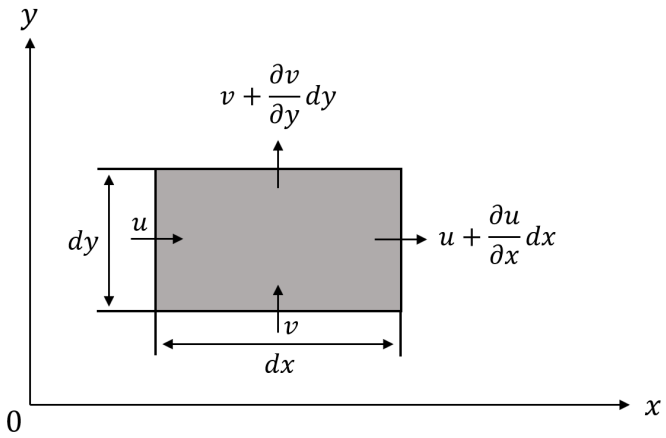

Figure 2.1: The spacial change in velocity over a fluid element of dx by dy. Figure inspired by [14, pg. 84].

progress in time but also on the displacement in space (as can be seen in figure 2.1). Thus du in the x-direction can be expressed as:

$$du = \frac{\partial u}{\partial t} dt + \frac{\partial u}{\partial x} dx + \frac{\partial u}{\partial y} dy. \tag{2.2}$$

Then the time derivative of u becomes:

$$\begin{aligned} \frac{du}{dt} &= \frac{\partial u}{\partial t} + \frac{\partial u}{\partial x}\frac{dx}{dt} + \frac{\partial u}{\partial y}\frac{dy}{dt} \\ &= \frac{\partial u}{\partial t} + u\frac{\partial u}{\partial x} + v\frac{\partial u}{\partial y}\,. \end{aligned} \tag{2.3}$$

This is equivalent for the velocity v in the y-direction. If we insert this into equation (2.1) we obtain:

$$\begin{aligned} \rho\, b\, dx\, dy \left(\frac{\partial u}{\partial t} + u\frac{\partial u}{\partial x} + v\frac{\partial u}{\partial y}\right) &= dF_x \\ \rho\, b\, dx\, dy \left(\frac{\partial v}{\partial t} + u\frac{\partial v}{\partial x} + v\frac{\partial v}{\partial y}\right) &= dF_y\,. \end{aligned} \tag{2.4}$$

The exerted forces on the fluid element can be categorized into two types:

1. **Body forces**, that act on the entire mass of the body.
2. **Surface forces**, that act on the surface of the body.

For the goal of this thesis body forces in the Navier-Stokes equations can be neglected and will not be addressed further in this section.
Examples of surface forces are pressure forces and viscous forces. These are external stressors

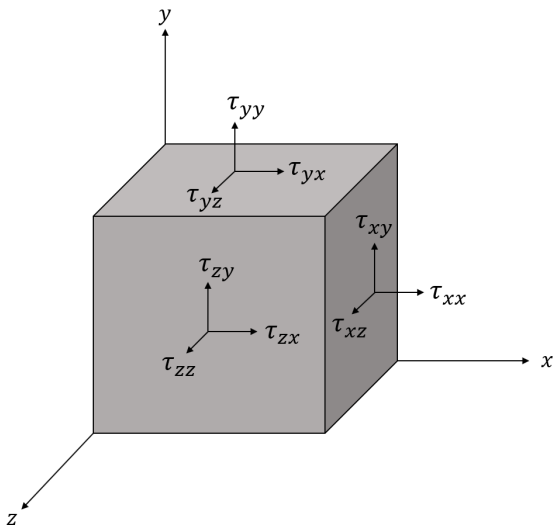

Figure 2.2: All different stress components for a 3-dimensional fluid element. Figure inspired by [15, pg. 63].

that act on the sides of our fluid element. Pressure and viscous forces can be separated in different terms, which then changes our equation (2.4) into the following:

$$\begin{aligned} \rho\, b\, dx\, dy \left(\frac{\partial u}{\partial t} + u\frac{\partial u}{\partial x} + v\frac{\partial u}{\partial y}\right) &= P_x + V_x \\ \rho\, b\, dx\, dy \left(\frac{\partial v}{\partial t} + u\frac{\partial v}{\partial x} + v\frac{\partial v}{\partial y}\right) &= P_y + V_y\,, \end{aligned} \tag{2.5}$$

with P_i the pressure forces and V_i the viscous forces that are exerted on the fluid element in the given i-direction. In the next section these surface forces will be derived.

Surface forces

The aforementioned external stressors, i.e. the surface forces that act on the fluid element, can be written as a stress tensor τ [5]. If we were to look at a 3-dimensional object the stress tensor would be composed from all the components shown in figure 2.2.

The fluid element in figure 2.2 gives us the following 3x3-matrix:

$$\tau = \begin{pmatrix} \tau_{xx} & \tau_{xy} & \tau_{xz} \\ \tau_{yx} & \tau_{yy} & \tau_{yz} \\ \tau_{zx} & \tau_{zy} & \tau_{zz} \end{pmatrix}\,. \tag{2.6}$$

This tensor is symmetric and thus $\tau_{ij} = \tau_{ji}$. Because we will be looking at problems where we can reduce the dimensionality with symmetry, we will continue with a stress tensor τ in 2D:

[5] With τ_{ij} the stress-component in the j-direction on a surface that is normal to the i-direction

$$\tau = \begin{pmatrix} \tau_{xx} & \tau_{xy} \\ \tau_{yx} & \tau_{yy} \end{pmatrix} . \tag{2.7}$$

The positions of the components in the stress tensor correspond to the applied force in each coordinate direction [15]. If we look at the surfaces that are visible in figure 2.2 then the total force in the x- and y-direction can be expressed as:

$$\begin{aligned} dF_x &= \tau_{xx}\, dy\, b \;+\; \tau_{xy}\, dx\, b \\ dF_y &= \tau_{xy}\, dy\, b \;+\; \tau_{yy}\, dx\, b\,. \end{aligned} \tag{2.8}$$

If our fluid element were to be in equilibrium, the total force on the back of the block element in figure 2.2 has to be equal and opposite in direction to the force on the front of the block. Though, if the fluid element where to be moving, there is a net force because of the differences between the front and back surfaces. The difference between these surfaces can be expressed for every component as:

$$\tau_{xx,\,\text{front}} = \tau_{xx,\,\text{back}} + \frac{\partial \tau_{xx}}{\partial x} dx\,. \tag{2.9}$$

Then we can write the net force in each direction as:

$$\begin{aligned} dF_{x,\,\text{net}} &= \left(\frac{\partial \tau_{xx}}{\partial x} dx\right) dy\, b + \left(\frac{\partial \tau_{yx}}{\partial y} dy\right) dx\, b \\ dF_{y,\,\text{net}} &= \left(\frac{\partial \tau_{xy}}{\partial x} dx\right) dy\, b + \left(\frac{\partial \tau_{yy}}{\partial y} dy\right) dx\, b\,. \end{aligned} \tag{2.10}$$

When the fluid element is at rest, all the shear stresses (the off-diagonal components) are equal to zero, and the normal stresses become equal to the hydrostatic pressure p:

$$\tau_{ii} = -p \quad \text{and} \quad \tau_{ij} = 0 \text{ for } i \neq j\,. \tag{2.11}$$

In the next step we will relate the stress components to the velocity of the fluid. This can be achieved with the help of the assumption that our fluid is a Newtonian fluid. Similar to Hooke's law, we are looking for a linear law for the viscous stress related to the strain rate as a first order approximation. The fluids that satisfy this relation are referred to as Newtonian fluids.
Blood as a solid-liquid mixture has to be considered a non-Newtonian fluid, which behaves differently depending on e.g. the dimensions of the vessels and the amount of particles present in the blood, making it a very difficult fluid to describe (see section 2.1 for a full explanation). However, since on a microscopic scale the size of the microbubbles ($\sim$3 μm) is considerably smaller that the average distance of the red-blood cells, we can assume as a first order approximation the immediate vicinity of the microbubbles as a Newtonian fluid. Nevertheless, it is important to keep in mind, that for interactions exceeding $5 - 10$ μm this

assumption is increasingly not valid.
A Newtonian fluid must satisfy the following:

1. The fluid must be continuous and $\tau \sim \epsilon$, with ϵ the strain-rate tensor.
2. The fluid is isotropic.
3. The deformation law must reduce to equation (2.11) when there is no strain rate.

The strain-rate tensor ϵ is related to velocity as follows:

$$\epsilon = \begin{pmatrix} \epsilon_{xx} & \epsilon_{xy} \\ \epsilon_{yx} & \epsilon_{yy} \end{pmatrix} \quad \text{with} \quad \epsilon_{ii} = \frac{\partial V_i}{\partial i}\,, \quad \epsilon_{ij} = \frac{1}{2}\left(\frac{\partial V_j}{\partial i} + \frac{\partial V_i}{\partial j}\right) \quad \text{for } i \neq j\,, \tag{2.12}$$

where V_i are the velocity components of the velocity vector $\mathbf{V}$.

With the above mentioned conditions we can derive the following expression for the stress tensor components [6]:

$$\tau_{ij} = -p\delta_{ij} + \mu\left(\frac{\partial V_i}{\partial j} + \frac{\partial V_j}{\partial i}\right) + \delta_{ij}\,\lambda\,\mathrm{div}\mathbf{V}\,, \tag{2.13}$$

with μ the coefficient of viscosity of a Newtonian fluid, λ the bulk viscosity of the Newtonian fluid and δ_{ij} the Kronecker delta function.

In all following problems the fluid is assumed to be incompressible. For an incompressible fluid the following is true:

$$\mathrm{div}\mathbf{V} = \mathbf{0}\,.$$

This will reduce equation (2.13) to:

$$\tau_{ij} = -p\delta_{ij} + \mu\left(\frac{\partial V_i}{\partial j} + \frac{\partial V_j}{\partial i}\right)\,. \tag{2.14}$$

If we then assume that the viscosity μ is constant, and is thus independent of pressure or temperature, we have found our expressions for the net force in the x- and y-direction of equation (2.10):

$$\begin{aligned} dF_{x,\,\mathrm{net}} &= -\frac{\partial p}{\partial x}\,dx\,dy\,b + \mu\left(\frac{\partial^2 u}{\partial x^2} + \frac{\partial^2 u}{\partial y^2}\right)\,dx\,dy\,b \\ dF_{y,\,\mathrm{net}} &= -\frac{\partial p}{\partial y}\,dx\,dy\,b + \mu\left(\frac{\partial^2 v}{\partial x^2} + \frac{\partial^2 v}{\partial y^2}\right)\,dx\,dy\,b\,. \end{aligned} \tag{2.15}$$

[6] For the full derivation see page 65-66 of [15].

As last step we take these expressions for the net surface force and substitute them into equation (2.4). If we devide everything by $dy\,dx\,b$ we obtain our final result:

$$\begin{aligned} \rho\left(\frac{\partial u}{\partial t}+u\frac{\partial u}{\partial x}+v\frac{\partial u}{\partial y}\right) &= -\frac{\partial p}{\partial x}+\mu\left(\frac{\partial^2 u}{\partial x^2}+\frac{\partial^2 u}{\partial y^2}\right) \\ \rho\left(\frac{\partial v}{\partial t}+u\frac{\partial v}{\partial x}+v\frac{\partial v}{\partial y}\right) &= -\frac{\partial p}{\partial y}+\mu\left(\frac{\partial^2 v}{\partial x^2}+\frac{\partial^2 v}{\partial y^2}\right). \end{aligned} \tag{2.16}$$

These are the 2-dimensional Navier-Stokes equations of a incompressible fluid for a constant viscosity in Cartesian coordinates. Most of the problems with microbubbles are better described in spherical or cylindrical coordinates due to the symmetries in the system. Depending on that system it might be a 2-dimensional or a 1-dimensional problem. In Appendix B, all 3-dimensional Navier-Stokes equations are given in Cartesian, Cylindrical and Spherical coordinates.

The Navier-Stokes equations represent a set of non-linear partial differential equations, which are generally hard to solve. The following section introduces how this equation system can be simplified for a single bubble with spherical symmetry.

2.3 Rayleigh-Plesset equation

For small oscillation amplitudes, an oscillating bubble can be approximated as a linear oscillator. A lot can be learned from bubble dynamics with a linear theory, e.g. the resonance frequency and damping constant. However, both in diagnostic as well as therapeutic applications employ higher pressure levels, which in turn requires an understanding in the physics of the non-linear dynamics of microbubbles. Solving these types of problems is a lot more difficult than the linear ones and ask for more complicated mathematics. One of the first non-linear differential equations that described the non-linear motion of a bubble in a fluid is now referred to as the *Rayleigh-Plesset equation*. It describes the dynamics of a bubble undergoing a spherically symmetric oscillation in an infinite fluid domain. This equation represents the first theoretical description on non-linear oscillations, which had been experimentally evidenced since the mid-nineteenth century as a problem for high-power ship propellers. Because of the importance of this equation in bubble dynamics we will shortly derive the Rayleigh-Plesset equation in this section. For a more complete derivation see [16].

Consider a spherically oscillating bubble with radius $a(t)$. This bubble exist in a infinite domain of a Newtonian inviscid fluid. Far away from the bubble the temperature T and pressure $p(t)$ are assumed to be T_∞ and $p_\infty(t)$. The temperature is assumed to be constant since no thermal effects or heat exchange are taken into account in this calculation. The pressure $p_\infty(t)$ is assumed to be known and is the input parameter that will cause the bubble to expand and collapse. It is furthermore assumed that the fluid is incompressible and that the density ρ_L and the viscosity μ_L of the fluid are constant and uniform. Lastly, it is assumed that there is zero mass transport across the bubble-fluid interface and that the content, the temperature $T_B(t)$ and pressure $p_B(t)$ within the bubble are uniform [17]. Figure 2.3 shows the above described situation.

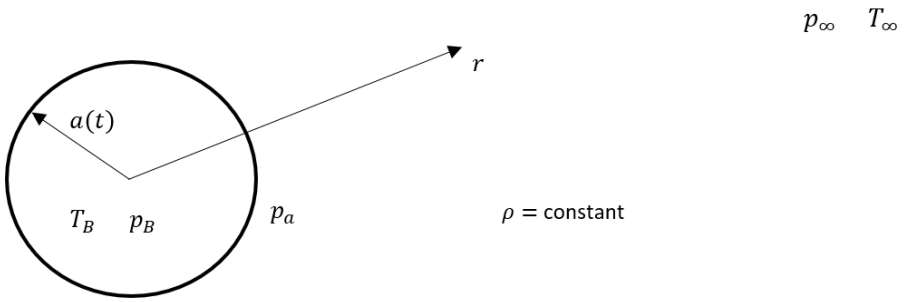

Figure 2.3: An illustration of an oscillating bubble in an infinite domain of fluid. Here $a(t)$ is the changing bubble radius, T_B and p_B are the temperature and pressure inside the bubble, p_a is the pressure at the bubble-fluid interface and T_∞ and p_∞ are the temperature and pressure far away from the bubble. The density ρ of the fluid is constant. Figure inspired by [16, pg. 55].

Because of the symmetry of the oscillation of the bubble and the dimensions of the fluid, the problem is reduced to one-dimension. The Navier-Stokes equations in spherical

coordinates (see appendix B) then reduces to:

$$\rho\left(\frac{\partial u}{\partial t}+u\frac{\partial u}{\partial r}\right)=-\frac{\partial p}{\partial r}\,, \tag{2.17}$$

with u the velocity in the r-direction. The viscous terms in the Navier-Stokes equation are dropped since the fluid is assumed to be inviscid. Now we integrate our reduced Navier-Stokes equation over the streamline from the bubble surface to infinity.

$$\int_{a(t)}^{\infty}\left(\frac{\partial u}{\partial t}+u\frac{\partial u}{\partial r}\right)dr=\frac{p_a-p_\infty}{\rho}\,, \tag{2.18}$$

with p_a the pressure at the bubble-fluid interface. The first term has a time-derivative inside the integral and a time-dependent integral boundary. To solve this we can use the Leibniz integration rule [18]:

$$\int_{a(t)}^{\infty}\left(\frac{\partial u}{\partial t}\right)dr=\frac{\partial}{\partial t}\int_{a(t)}^{\infty}u\,dr+u(a,t)\,\frac{\partial a(t)}{\partial t}\,. \tag{2.19}$$

The continuity equation is a statement for mass conservation in the system. Because we have a incompressible fluid, i.e. the density ρ of the fluid is constant, the continuity equation for this system is [12][7]:

$$\frac{\partial(ur^2)}{\partial r}=0\,. \tag{2.20}$$

With the continuity equation we can find an expression for the velocity u in terms of the position r:

$$\frac{\partial(u\,r^2)}{\partial r}=0\quad\longrightarrow\quad u=\frac{f(t)}{r^2}\,, \tag{2.21}$$

with $f(t)$ a function that still has to be determined. If we substitute this into the integral on the right-hand side of equation (2.19) we see that:

$$\begin{aligned}\frac{\partial}{\partial t}\int_{a(t)}^{\infty}\frac{f(t)}{r^2}\,dr &= \frac{d}{dt}\left(\frac{f(t)}{a(t)}\right)\\ &= \frac{\dot f\,(t)}{a}-\frac{f(t)\,\dot a}{a^2}\,,\end{aligned} \tag{2.22}$$

where we have used the dot notation to indicate time derivatives. In the evaluation of this integral, as $r\to\infty$ we see that $f(t)/r\to 0$. We can rewrite $f(t)$ with the expression that was found for u in equation (2.21):

[7] For a full derivation of the continuity equation see page 111-114 of [12].

$$\begin{aligned} f(t) &= u\,r^2 \\ \frac{f(t)}{dt} &= \dot{u}\,r^2 + 2u\,r\,\dot{r}\,. \end{aligned} \tag{2.23}$$

The $f(t)$ on the right-hand side in equation (2.22) is evaluated at $r = a(t)$. Now that we have found $f(t)$ expressed in terms of u and r we can evaluate it at $a(t)$ and plug it all back into equation (2.19) (in the previously mentioned dot notation):

$$\int_{a(t)}^{\infty} \left(\frac{\partial u}{\partial t}\right) dr = \frac{\ddot{a}a^2 + 2a\dot{a}^2}{a}\,, \tag{2.24}$$

Finally we can take this and insert it back into the integrated Navier-Stokes equation:

$$a\ddot{a} + \frac{3}{2}\dot{a}^2 = \frac{p_a - p_\infty}{\rho}\,. \tag{2.25}$$

This gives us the Rayleigh-Plesset equation. The pressure at the bubble-fluid interface is determined with the characteristic of the bubble shell and the bubble content. The Rayleigh-Plesset equation in this form is very useful because it can be used for different types of microbubbles with different types of bubble shell and bubble content without having to change the equation drastically. One just computes p_a for their bubble and can use this equation instantly. With p_a and p_∞ known, the differential equation can be solved for $\ddot{a}$. This results in the changing radius a with time for an oscillating pressure field p_∞. The oscillating pressure field is often written as:

$$p_\infty = p_0 + p_i(t)\,, \tag{2.26}$$

with p_0 the equilibrium pressure far away from the microbubble, and $p_i(t)$ a deviation from this equilibrium pressure which signifies the oscillating field we apply to it.

Because the Rayleigh-Plesset equation is such a widely used equation in this field of physics, and because it is fairly easy to compute numerically, the goal of our simulation is to formulate a differential equation for an oscillating microbubble in a rigid tube that has a similar form to the Rayleigh-Plesset equation and can be solved similarly.

2.4 Shell Model

In this thesis we will be looking at the oscillation of microbubbles with a specific type of coating around it, referred to as microbubble contrast agents. Thus, a shell model needs to be formulated to simulate the effects that the coating will have on the microbubbles' reaction to the ultrasound wave. The shell model gives the pressure p_a at the bubble-fluid interface that is needed in the Rayleigh-Plesset equation (2.25).
Most of the shell models that have been defined, have been formulated for a specific type of contrast agent, because their mechanics differ considerably depending on the material they

are made of. In recent years new shell models have been formulated that might improve these models for some contrast agents, though we won't go into the physics of all different contrast agents in this section. The PHD thesis by M. Emmer [19] and a paper by Doinikov et al. [20] both give a good overview of a selection of different shell models that have been developed in the previous decades.

The one we will be using is the shell model by Hoff et al. [21]. This shell model has often been used to simulate the shell of the contrast agent Sonovue®. We will not validate if this shell model is best to simulate Sonovue and will assume it to do so. Hoff's model is an approximation of the shell model by Church [22]. This linear shell model is made for a visco-elastic shell material:

$$p_a = -4\mu_L \frac{\dot{a}}{a} - 12\mu_s \frac{d_s\, a_0^2}{a^3}\,\frac{\dot{a}}{a} - 12G_s \frac{d_s\, a_0^2}{a^3}\left(1 - \frac{a_0}{a}\right) + p_e\left(\frac{a_0}{a}\right)^{3\kappa}, \tag{2.27}$$

where a_0 is the bubble radius at equilibrium, d_{Se} is the shell thickness, μ_L is the fluid shear viscosity, μ_s is the shell shear viscosity and G_s is the shells shear modulus. The shear modulus G_s and the shear viscosity μ_s are to be taken constant here. In the last term on the right, p_e is the pressure in the microbubble when no pressure field is added and κ is the polytropic gas constant.
Within this model two assumptions were made about the shell. First, that it is thin compared to the radius of the microbubble. Secondly, that the shell material is incompressible. The surface tension is neglected because it is assumed the shell will reduce the surface tension at both the inner- an outer-bubble interfaces. Considering that the surface tension of blood, where the microbubbles will be diluted in once inserted into the body, is low compared to water, this considered an acceptable estimate.

In his work *Acoustic Characterization of Contrast Agents for Medical Ultrasound Imaging* [16] (published a year after publishing his model in equation (2.27)), Hoff postulated a exponential relation between the pressure and the radial strain and viscosity. Though he stated that deciding which model simulates the best response must be done by experiments, he used this exponential shell model in his own MATLAB simulation. For his motivation of this postulate see section 3.4 in [16].
Because we will be comparing our own model to the model written in this MATLAB simulation, we will also use the exponential shell model:

$$p_a = -4\mu_L \frac{\dot{a}}{a} - 12\frac{d_s}{a_0}\left(G_s x_0\left(1 - e^{-\left(\frac{a}{a_0}-1\right)/x_0}\right) + \mu_s\, e^{-\left(\frac{a}{a_0}-1\right)/x_1}\frac{\dot{a}}{a_0}\right) + p_e\left(\frac{a_0}{a}\right)^{3\kappa}, \tag{2.28}$$

with $x_0 = \frac{1}{8}$ and $x_1 = \frac{1}{4}$.[8]

[8] For an explanation of the estimates of these constants see section 3.4.2 and 3.4.3 of [16].

2.5 Poiseuille flow theory

One of the downsides of the Rayleigh-Plesset equation is that it is defined for a infinite domain of fluid. Although, this is appropriate for a single bubble in a large volume of fluid, for bubbles inside small(er) capillaries it is increasingly inaccurate, since the wall interaction of the fluid is neglected. For this reason we want to find a new differential equation that will describe the motion of a bubble inside a tube. As mentioned before in section 2.2, the Navier-Stokes equations represent a complex mathematical problem with only a limited number of solutions for specific, in general rather simple, cases. Fortunately, the historical interest and relevance of hydraulic problems directed a considerable effort into solving the problem of laminar flow in a tube. This theory, the Poiseuille flow theory, will be our starting point for the theoretical description of oscillatory motion of a bubble inside a tube. We will start by a brief introduction into this theory.

For the derivation of Poiseuille flow inside a tube we largely follow the explanation given in section 8.2 from the book *Incompressible Viscous Flows* by Fang [23] and section 6.3 from the book *Introduction to Fluid Mechanics* by Nakayama and Boucher [14].

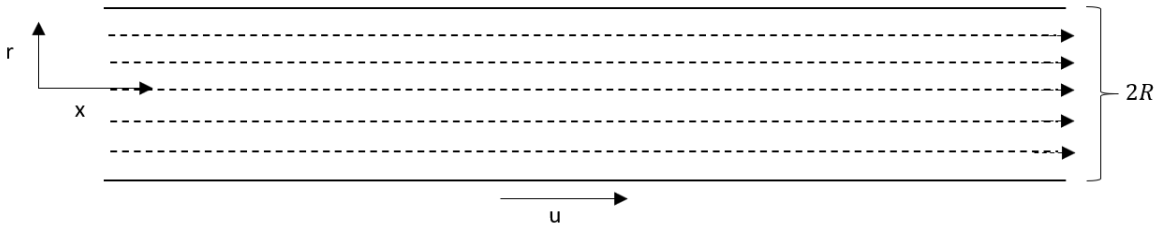

Figure 2.4: Laminar flow through a pipe of radius R. The velocity u of the flow is in the x-direction.

We are looking at a fully developed steady laminar flow inside a tube. Because of the symmetry of the tube, a cylindrical coordinate system for the Navier-Stokes equation is preferred. Figure 2.4 shows the orientation of the tube to the coordinate system. Because we are dealing with laminar flow there is only a fluid flow u in the x-direction. Due to the axial symmetric flow, the Navier-Stokes equation reduces to[9]:

$$\frac{1}{r}\frac{d}{dr}\left(r\frac{du}{dr}\right) = \frac{1}{\mu}\left(\frac{dp}{dx}\right) . \tag{2.29}$$

Note that the right-hand side of the equation is independent of r. Therefore, we can integrate this twice over r and see that:

$$u(r) = \frac{1}{\mu}\left(\frac{dp}{dx}\right)\frac{r^2}{4} + C_1 \ln r + C_2 , \tag{2.30}$$

[9]For this reduced Navier-Stokes equation we have again used the Continuity equation for a compressible fluid. For the derivation of this equation see page 111-114 of [12].

with C_1 and C_2 the integration constants. To determine these constants we have to look at the boundary conditions of our system. For $r = 0$ we expect the velocity u to have some finite value, and thus the constant C_1 has to be equal to zero, $C_1 = 0$. For $r = R$ we use the no slip boundary condition that the velocity u at this boundary wall has to be zero, which means that the solution for C_2 yield then that $C_2 = -(dp/dx)R^2/(4\mu)$. Thus equation (2.30) is expressed as:

$$u(r) = -\frac{1}{4\mu}\left(\frac{d\,p}{d\,x}\right)\left[R^2 - r^2\right] . \tag{2.31}$$

This equation gives us the flow profile in the tube. The change in velocity in the r-direction has a parabola shape as can be seen in figure 2.5. Thus depending on the distance from the centerline of the tube the velocity changes. Because of this parabolic shape the maximum velocity inside the tube is on the centerline, where $r = 0$:

$$u_{max} = -\frac{R^2}{4\mu}\left(\frac{d\,p}{d\,x}\right) . \tag{2.32}$$

Another usefull parameter is the mean flow velocity in the tube. The mean flow velocity $\bar{v}$ can be determined by calculating the volumetric flow rate Q of the tube and dividing it by the cross section (with the assumption that there is only flow in one direction inside the tube).

$$Q = \int_0^R 2\pi\, r\, u\, dr = -\frac{\pi R^4}{8\mu}\frac{d\,p}{d\,x} . \tag{2.33}$$

Here we have used the flow velocity $u(r)$ that was determined in equation (2.31). Now the mean flow velocity becomes:

$$\bar{v} = \frac{Q}{2\pi R} = -\frac{R^2}{8\mu}\frac{d\,p}{d\,x} = \frac{1}{2}\,u_{max} , \tag{2.34}$$

where we have noted that the mean velocity is half the maximum velocity inside the tube.

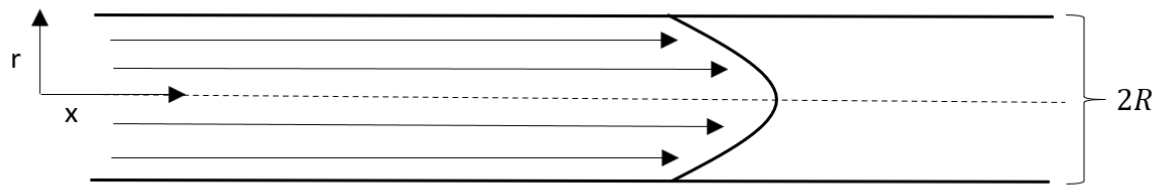

Figure 2.5: A parabolic flow profile inside a tube with radius R.

Due to the viscosity of the fluid it exercises shear stresses on the boundaries of the tube. Due to these shear stresses there arises a pressure drop Δp inside the tube, also called the *head loss* H_l. This is an important phenomena of fluid flow inside tubes and is called the Hagen-Poiseuille formula. Here we want to express the pressure drop Δp in length Δx of the tube. We can do this by combining equations (2.32), (2.33) and (2.34):

$$\Delta p = H_l = \frac{32\,\mu\,\bar{v}}{D^2}\Delta x\,, \tag{2.35}$$

with D the diameter of the tube.

In the next section we will try to combine this theory and the Rayleigh-Plesset equation to get a differential equation that will simulate the oscillation of an microbubble inside a rigid tube.

3 Method

In this section we will derive a differential equation that will combine the Rayleigh-Plesset equation with Poisseuille flow theory. This equation is based upon two papers by Qamar et al. [11][24]. Once the differential equation is derived, it is shortly explained how to simulate it in a program called MATLAB. The form of this simulation is comparable and inspired by the microbubble oscillation simulation, BubbleSim, written by Hoff (see [16]). Lastly, the simulation is validated with two different tests.

3.1 Deriving differential equation

In this section we will derive the differential equation that will simulate the oscillation of a microbubble inside a rigid tube. The derivation of this model is given step by step, which largely follows the one given in the paper by Qamar et al. [24]. It should be noted that a lot of assumptions will be made to simplify the model in such a way that it can be easily simulated similar to Hoff's simulation, Bubblesim [16].

The setup as seen in figure 3.1 will be used for this numerical simulation. A microbubble of initial radius a_o will oscillate in the middle of a rigid tube with diameter D and length L. The pressure at the bubble-fluid interface is p_a, and the pressure at the end of the tube is $p_{l/2}$. The dimensional parameters that we will choose, shall represent those of capillaries in the brain and the bubble size distribution of Sonovue®.
Simulating a microbubble within an tube is more complicated then simulating one in an infinite fluid domain. The Rayleigh-Plesset equation is based upon a inviscid fluid where the boundaries are placed at infinity (see section 2.3 for this full derivation). In order to incorporate the physics of a tube, the change in symmetry of the system has to be taken into account and the fluid can not be considered as inviscid because of the fluid's interaction with the inside of the tube. If the full flow field were to be calculated one would need to solve equation (2.16) in its entirety.

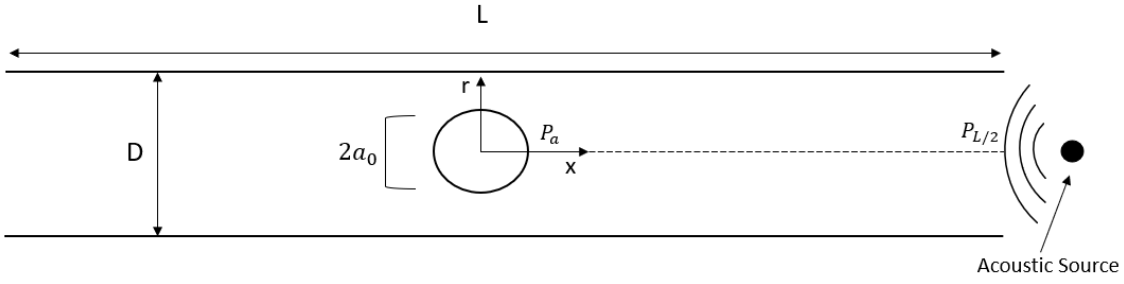

Figure 3.1: A visual repesentation of the system that will be simulated with the derived differential equation: A microbubble oscillating in the middel of a rigid tube. The tube has length L and diameter D. The microbubble has an initial radius of a_0. The pressure at the bubble-fluid interface is P_a, the pressure at the end of the tube is $P_{L/2}$. The acoustic source is placed at the end of the tube. Model inspired by one in [11].

Due to the complexity of these non-linear differential equation there are no general solution available. This is why we will make some assumptions about our model. Because of this, the differential equation that is obtained from this approach is in no means an exact description of reality, but it will nevertheless suffice to theoretically analyze the fundamental properties of the system, as the experimental validation by Qamar et al. [11] has shown.

For our model we will be considering an incompressible inviscid laminar flow, where some viscous effects will be added later, inside a rigid tube with no body forces working on the system. The microbubble is assumed to oscillate spherically symmetric in the centre of the tube. This is a coarse assumption, since it has been shown in experiments that microbubbles inside a tube deviate from spherically symmetric oscillation due to the orientation of the tube [25]. The bubbles are more elongated in the x-direction during oscillation. There are indications that this deviation from spherical symmetric oscillation depends on the ratio between the diameter of the tube and the microbubble, and on the wall velocity of the bubble. Previous research has shown that for small vessel/bubble diameter ratios this anti-symmetric bubble oscillation becomes significant, and even for larger ratios with high wall velocities it becomes an important part of the oscillation [26]. Because we will be looking at oscillations in capillaries, where the diameter of the tube and the bubble are of the same order of magnitude, assuming only spherically symmetric oscillations becomes inaccurate. This has to be kept into consideration when looking at the results of this research.

Another assumption is that the bubble is oscillating in the centre of the tube. This means that we are neglecting translational propagation by radiation forces (or Bjerknes forces) and the pulsating flow of blood in our model. Both of these phenomena interact on a larger timescale then the oscillation of the microbubble, since the microbubble oscillates predominantly with the principal frequency, which is in the order of MHz. Thus, not including these translational propagation is a good assumption for short pulses of the transmitted wave . Though, the longer the transmitted wave, the more inaccurate this assumption becomes.

At last, no external interactions were taken into account. Even though the microbubbles have a low density once injected in the blood (thus making interaction between them relatively small), there are a lot of other particles in the blood of the same order of magnitude with which they can interact, e.g. red blood cells. Depending on the concentration of these particles in the blood and their exact size, they will interact differently with each other.

Instead of solving the entire flow field inside the tube, we will only be solving it along the centerline streamline inside the tube. Because of the symmetry that was created in this model, the flow field on the centerline will be symmetric. This means that the fluid particles that are travelling along the centerline streamline will be irrotational (i.e. in absence of vorticity).
If we integrate the Navier-Stokes equation over the centerline streamline, by taking the assumptions made in this section into account, we get a differential equation that describes the spherical oscillation of the microbubble. In the next part of this section we will be deriving this differential equation.

The Navier-Stokes equation derived in section 2.2 will reduce to the following form (in cylinderical coordinates):

$$\begin{aligned} \rho\left(\frac{\partial u}{\partial t} + u\frac{\partial u}{\partial x}\right) &= -\frac{\partial p}{\partial x} \\ 0 &= -\frac{\partial p}{\partial r}\,, \end{aligned} \tag{3.1}$$

where u is the flow velocity in the x-direction, ρ is the density of the fluid and p is the pressure inside the tube. From this we can already tell that the pressure p inside the tube is only dependent of displacement x and time t: $p = p(x,t)$. Now we integrate along the centerline streamline:

$$\int_{a(t)}^{L/2}\left(\frac{\partial u}{\partial t} + u\frac{\partial u}{\partial x}\right)dx + \frac{H_L}{\rho} = \frac{p_a - p_{L/2}}{\rho}\,, \tag{3.2}$$

where we have integrated from the surface of the microbubble $a(t)$ to the end of the tube $L/2$. The H_L term added in this equation is a compensation for the assumption that we are dealing with an inviscid fluid. Though this assumption might be a correct one to make for the Rayleigh-Plesset equation, for fluid flow inside a tube it is not. As can be read in section 2.5, the viscosity of the fluid inside the tube gives a distinct flow profile inside the tube and a pressure loss arises due to viscous forces at the boundaries. To include these effects we add a total pressure loss (or head loss) H_L to our equation. This is a very blunt way of doing this but gives us an easier equation to deal with that still, in some approximation, accounts for the viscosity of the fluid. The integration over the streamline is taken inside the head loss term H_L.

Some parts of the integration in equation (3.2) can immediately be solved, which turns equation (3.2) into:

$$\int_{a(t)}^{L/2}\left(\frac{\partial u}{\partial t}\right)dx + \frac{1}{2}\left(u_{L/2}^2 - u_a^2\right) + \frac{H_L}{\rho} = \frac{p_a - p_{L/2}}{\rho}. \tag{3.3}$$

Other parts of this equation will need to be solved individually. The first term on the right-hand side has a time-derivative inside the integral and a time-dependent integral boundary. To solve this we can use the Leibniz integration rule [18]:

$$\int_{a(t)}^{L/2}\left(\frac{\partial u}{\partial t}\right)dx = \frac{\partial}{\partial t}\int_{a(t)}^{L/2} u\,dx \;+\; u(a(t),t)\frac{d\,a(t)}{dt}\,. \tag{3.4}$$

The first term on the left-hand side of the equation can be related to the average velocity flow $\bar{U}$ inside the tube with Poiseuille flow theory. This is because we are integrating along the centerline streamline, and thus the velocity along this line can be expressed by equation (2.34). The second term on the right-hand side can be seen as the square of the velocity in point $a(t)$:

$$\int_{a(t)}^{L/2} \left(\frac{\partial u}{\partial t}\right) dx = 2\left[\frac{L}{2} - a\right] \frac{d\bar{U}}{dt} + u(a(t), t)^2 \,. \tag{3.5}$$

Now with mass conservation we can find a relation between the average velocity flow $\bar{U}$ and the bubble surface $a(t)$:

$$\frac{d}{dt}\left(\frac{\pi D^2}{4} - \frac{4\pi a^3}{3}\right) = -\beta \bar{U} \frac{\pi D^2}{4} \,. \tag{3.6}$$

This equation states that the change in volume of the fluid inside the tube (left-hand side) must be equal to the flow rate through the cross section at the ends of the tube (right-hand side). If the tube has one opening, β will be equal to 1, and if the tube has two openings, β will be equal to 2.

From equation (3.6) we can get an expression for $\bar{U}$ and the time derivative of $\bar{U}$:

$$\bar{U} = \frac{16a^2}{\beta D^2} \frac{d\,a}{dt} \,, \tag{3.7}$$

$$\frac{d\bar{U}}{dt} = \frac{16}{\beta D^2}\left[a^2 \frac{d^2 a}{dt^2} + 2a\left(\frac{da}{dt}\right)^2\right] \,. \tag{3.8}$$

The next term we will need to determine is the fluid velocity on the streamline at the end of the tube (see the second term in equation 3.3). In reality the change of velocity in this point depends om the change of the pressure in $a(t)$ and the velocity at which this pressure change travels from point $a(t)$ to the end of the tube at $L/2$. To make our problem more easily solvable we make an approximation here. Even though the whole system is unsteady, we will determine the velocity at the end of the tube as if it was a steady problem. This means that the pressure changes instantaneous from the bubble surface to the end of the tube. In other words, we are looking at a lot of alternating steady flows where the change from one to the other is instantaneous. This approximation is justified because we are working with an incompressible fluid. Doing this, we can use Poiseuille flow theory to determine $u(L/2, t)$ (described in section 2.5):

$$u(r, t) = -\frac{1}{4\mu}\frac{dp}{dx}\left(\frac{1}{4}D^2 - r^2\right) \,, \tag{3.9}$$

with dp/dx the change in pressure along the streamline, r the radial coordinate of the streamline and μ the viscosity of the fluid inside the tube. We are integrating over the centerline, thus $r = 0$ and the velocity becomes:

$$u_{L/2} = -\frac{1}{16\mu}\frac{dp}{dx} D^2 \,. \tag{3.10}$$

The change in pressure along the length of the tube can be approximated by:

$$\frac{d\,p}{d\,x} \approx \frac{p_{L/2} - p_a}{L/2 - a}\,. \tag{3.11}$$

The head loss term we added in equation (3.3) can now also be determined from Poiseuille flow theory:

$$\frac{H_L}{\rho} = \frac{32\,\mu\,\bar{U}}{\rho\,D^2}\Delta x\,. \tag{3.12}$$

Here, Δx is the length of the tube over which was integrated. Using the expression for $\bar{U}$ we found earlier and using the dimensions of our problem we get that:

$$\frac{H_L}{\rho} = \frac{512\mu a^2}{\beta\rho D^4}\frac{da}{dt}\left[\frac{L}{2} - a\right]\,. \tag{3.13}$$

Now we can insert all the expressions we found into equation (3.3) to get our final result. Here is a dot notation used for all the time derivatives:

$$\frac{32}{\beta D^2}\left[\frac{L}{2} - a\right]\left[a^2\ddot{a} + 2a\dot{a}^2\right] + \dot{a}^2 + \frac{1}{2}\left(\frac{D^4}{256\mu^2}\left(\frac{p_{L/2} - p_a}{L/2 - a}\right)^2 - \dot{a}^2\right)$$

$$+\frac{512\mu_L a^2}{\beta\rho D^4}\dot{a}\left[\frac{L}{2} - a\right] = \frac{p_a - p_{L/2}}{\rho}\,. \tag{3.14}$$

The pressure at the bubble surface can be expressed by the shell model by Hoff (as describes in section 2.4):

$$\begin{aligned} p_a &= -4\mu_L\frac{\dot{a}}{a} + p_s + p_g \\ p_s &= -12\frac{d_s}{a_0}\left[G_s\,x_0\left(1 - e^{-(a/a_0-1)/x_0}\right) + \mu_s\,e^{-(a/a_0-1)/x_1}\frac{\dot{a}}{a_0}\right] \\ p_g &= p_e\left(\frac{a}{a_0}\right)^{-3\kappa}\,. \end{aligned} \tag{3.15}$$

The different viscosities are distinguished in these equation by μ_L for the viscosity of the fluid and μ_s for the viscosity of the shell. p_s is the stress difference across the shell and p_g the pressure inside the bubble.

Equation (3.14) and (3.15) together make our non-linear differential equation that we will use to simulate the microbubble oscillation. The next sections will describe how these equations are to be used and how to write a script that will solve the oscillation and give the sub- and ultraharmonic response out of this signal.

3.2 Equation in dimensionless variables

To make the equation easier to compute for a solver, it is desired to write the differential equation (3.14) in dimensionless parameters. This way there are less parameters in the simulation which allows there to be a better control over the precision. It might also give some insight on the characteristic of our equation and problem.

The next dimensionless parameters are introduced into our equations:

$$\begin{aligned}
r &= \frac{a}{a_0} && \text{Radial strain} \\
L_0 &= \frac{L}{a_0} && \text{Normalized tube length} \\
D_0 &= \frac{D}{a_0} && \text{Normalized tube diameter} \\
t_c &= \sqrt{\frac{\rho\, a_0}{p_0}} && \text{Characteristic time} \\
\tau &= \frac{t}{t_c} && \text{Dimensionless time} \\
r' = \frac{dr}{d\tau} &= t_c \frac{dr}{dt} = t_c \dot{r} && \text{Time differentiation} \\
q &= \frac{p}{p_0} && \text{Normalized Pressure} \\
\nu_L &= \frac{\mu_L}{t_c\, p_0} && \text{Normalized Shear viscosity of liquid} \\
\nu_s &= \frac{\mu_s\, d_s}{t_c\, p_0\, a_0} && \text{Normalized viscosity of the shell} \\
g_s &= \frac{G_s\, d_s}{p_0\, a_0} && \text{Normalized modulus of the shell.}
\end{aligned} \tag{3.16}$$

With these we can rewrite our ODE and shell model into dimensionless parameters:

$$\begin{aligned}
\frac{32}{\beta D_0^2}\left[\frac{L_0}{2} - r\right]\left[r^2 r'' + 2\, r\, r'^{\,2}\right] + r'^{\,2} + \frac{1}{2}\left(\frac{D_0^4}{256\,\nu_L^2}\left(\frac{q_{L/2} - q_r}{L_0/2 - r}\right)^2 - r'^{\,2}\right) \\
+ \frac{512\,\nu_L\, r^2}{\beta D_0^4} r' \left[\frac{L_0}{2} - r\right] = q_r - q_{L/2}.
\end{aligned} \tag{3.17}$$

$$\begin{aligned} q_r &= -4\nu_L \frac{r'}{r} + q_s + q_g \\ q_s &= -12\left[g_s\, x_0\left(1 - e^{-(r-1)/x_0}\right) + \nu_s e^{-(r-1)/x_1}\, r'\right] \\ q_g &= q_e\, r^{-3\kappa} \end{aligned} \tag{3.18}$$

3.3 Determining driving pressure

Ultrasound is used to make the microbubbles oscillate. The change in pressure causes the bubble to expand and collapse. To determine how this will effect our system it is important to first determine where this driving pulse is coming from. Because we have translated our problem to one that is only defined on the centerline streamline, it is sensible to place the source of our driving pulse on this same line. This way, no changes have to be made in our equations. It is important to note though, that this is not similar to actual experimental or clinical setups. In most of those settings the source of the driving pulse is placed outside the body, without knowing its orientation relative to the capillaries in the body.

When we place the source at the end of our tube, we can say that the pressure at that point deviates from its equilibrium value with some small value p_i. This deviation is the driving pulse we put into our system:

$$p_{L/2} = p_0 + p_i(t), \tag{3.19}$$

with p_0 the equilibrium value of the pressure at the end of the tube. This change in pressure can be defined with a sine function:

$$p_i(t) = p_d\, \sin(2\pi f\, t), \tag{3.20}$$

with p_d the peak negative pressure (PNP) we drive the system with. Using the normalizations from 3.16 we can normalize the pressure as:

$$q_{L/2} = 1 + q_d \sin(f_0\, \tau). \tag{3.21}$$

With this expression for the oscillating driven field, we have everything to simulate the oscillation of the microbubble.

3.4 Numerical simulation

To get the results from our new model, we have to solve the derived differential equation. The scientific programming language MATLAB will be used to simulate our model and visualize our results. In the next sections, parts of the numerical code are explained and the parameters needed for our model are given.

ODE solver

MATLAB has build-in differential equation solvers to be readily used. Depending on the type of problem, there are different kind of solvers with different numerical strategies. The solver that was chosen for this problem is the so called *ode15s* solver, that uses a variable order method. This solver is preferable for stiff differential equation; an equation with large differences in scaling. In the *ode15s* solver, the time steps are determined by the local error that has to stay under a certain given tolerance level. Thus, not all time steps are of the same length.

The non-linear oscillation of a coated microbubble has a distinct form with a so called 'compression only' behavior (see figure 3.2). This non-linear phenomenon, though not discussed, is of importance to our simulation.

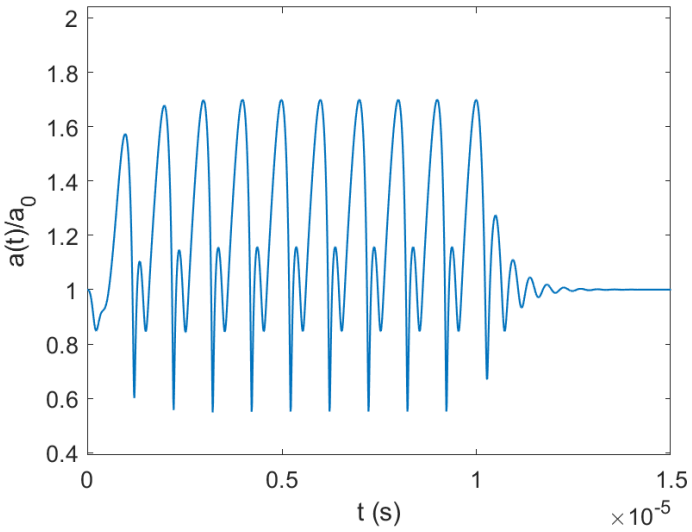

Figure 3.2: An example of 'Compression only' behavior, where we see a sharp and quick compression of the bubble radius and a slower expansion. This 10 cycle oscillation is for a microbubble with initial radius of $a_0 = 2$ micron, driving frequency of 1 MHz and PNP of 150 kPa. This was simulated with the Rayleigh-Plesset equation.

Depending on the parameters of the oscillation, this 'compression only' behavior can become too sharp for MATLAB to calculate. This occurs frequently for bubbles that have a resonance frequency close to the driving frequency, with pressures higher than 200 kPa. Because there is a fixed minimum time step, the error for some simulations becomes too great to simulate the oscillation correctly. These types of simulations will not be further studied,

and are excluded from the results.

Equation 3.17, rewritten to solve for r'', is used in the *ode15s* solver in MATLAB:

$$r'' = \frac{\beta\, D_0^2}{32\, r^2}\left[\frac{L_0}{2} - r\right]^{-1}\left[q_r - 1 - q_i(t) - \frac{r'^{\,2}}{2} - \frac{D_0^4}{512\,\nu_L^2}\left(\frac{1 + q_i(t) - q_r}{L_0/2 - r}\right)^2\right] - \frac{16\,\nu_L\, r'}{D_0^2} - \frac{2\, r'^{\,2}}{r} \tag{3.22}$$

Chosen parameters

As shown in equation 3.14 and 3.15, there are a lot of parameters needed to simulate our differential equation. The contrast agent that we will be simulating is Sonovue, and thus some parameters will be chosen to fit its characteristics. Other parameters are taken from literature or from assumptions made in the derivation of our model. All the parameters that stay constant in the simulations are listed in table 3.1.

Parameter description	**Parameter**	**value**
Density of fluid	ρ	1000 kg/m^3
Hydrostatic pressure	p_0	$1.013 \cdot 10^5$ Pa
Pressure inside bubble	p_e	p_0
Shear modulus of shell	G_s	$23 \cdot 10^6$ Pa
Shear viscosity of shell	μ_s	0.5 Pa $\cdot$ s
Shell thickness	d_s	$4.0 \cdot 10^{-9}$ m
Driving frequency	f	1 MHz
Number of outlets tube	B	2
Polytropic constant	κ	1

Table 3.1: The values of constant parameters that are used to simulate the microbubble oscillations.

Here we say that the equilibrium pressure inside the bubble is equal to the hydrostatic pressure p_0 of the liquid. We can say this because we assume that there is no tension on the shell at equilibrium and the surface tension is neglected (see section 2.4)[16]. The ploytropic constant κ depends on the frequency at which the system is driven. For low frequencies, the temperature in the bubble can be considered constant. This will give an isothermal oscillation, with $\kappa = 1$. For high frequencies the oscillation is adiabatic and $\kappa = \gamma$, with γ

the adiabatic index. For intermediate frequencies the oscillation is somewhere in between isothermal and adiabatic [10]. We already assumed that the temperature inside the bubble is constant and thus that our system is isothermal. All our simulations will be driven at a frequency of 1 MHz. All the other Sonovue shell parameters listed in table 3.1, as well as the bubble distribution shown in figure 3.3, were provided by the supervisor of this project [27].

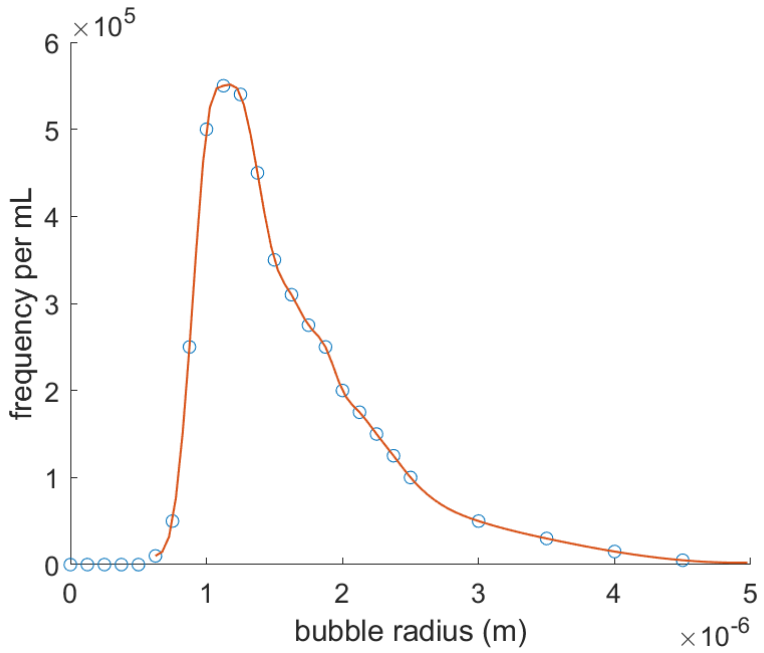

Figure 3.3: The bubble distribution per mL of the contrast agent Sonovue.

For the tube dimensions, viscosity μ_L of the fluid, microbubble radius and driving PNP, we choose a range of values to see what effect the change in these parameters will have on the oscillation of the system. The dimensions of the tube and viscosity of the liquid are chosen to reflect values that of blood and capillaries in the human brain.
Measuring the viscosity of blood in capillaries is experimentally very difficult and is often only done in larger vessels. Because we want to compare the change in dynamics due to deviation from the viscosity of water, we will look at a range of viscosities around that of water. We will look at $0.7 - 2.2$ mPas, with 1.0 mPas the viscosity of water at room temperature. We will be taking steps of 0.3 mPas. This range was also chosen to include the viscosity of bloodplasma, that is typically found in the range between 1.3 and 1.7 mPas [28].
There are a lot of different reports on the diameter range of calliparies vessels. The diameters differ for specific organs, and even within one organ they can vary between different regions. Some report a range of $4 - 8\mu$m [29], while others report capillaries up to a diameter of 20 μm[30]. Our model, however, appears to break down for large a_0/D ratios (also mentioned by Qamar et al. about this model [11]). This is why we will focus our analysis on a range of $10 - 20$ micron for the tube diameter. In the paper by Løkkegaard et al. [31], they report a mean capillary length between $97 - 115$ micron for the hippocampal region in the brain.

[10] A more lengthy explanation can be read in section 2.3 of [16].

The hippocampus is only a small region in the brain, and thus we extend this range and take $50 - 250$ micron.
The range in microbubble radii is chosen from the microbubble distribution of the contrast agent Sonovue, seen in figure 3.3. The range in PNP is chosen to be from 100 to 300 kPa. Table 3.2 shows a summary of the above chosen parameter ranges.

Description parameter	Parameter	Value range	Step size
Initial bubble radius	a_0	$0.6125 - 3$ micron	0.125 micron
Tube diameter	D	$10 - 20$ micron	2 micron
Tube length	L	$150 - 250$ micron	10 micron
Viscosity fluid	μ_L	$0.7 - 2.2$ mPa $\cdot$ s	0.3 mPa $\cdot$ s
Peak Negative Pressure (PNP)	p_d	$100 - 300$ kPa	10 kPa

Table 3.2: Range of values of parameters that are used to simulate the microbubble oscillations.

Calculating the harmonic responses

By calculating the discrete Fourier transfrom (DFT) of the radial oscillation, we can find in what frequencies the microbubble oscillates in response to the driving frequency. It will give us a frequency domain representation of the time domain oscillation. For non-linear oscillations we expect to see, besides the principal frequency with which the system is driven, higher harmonics that are integer multiples of the principal frequency. Other non-linear oscillation modes give rise to sub- and ultraharmonics seen in the frequency response of the bubble. These are the responses we are most interested in. Subharmonics are halve the principal frequency and ultraharmonics are higher harmonics of the subharmonic frequency. The DFT is computed in MATLAB with a function that uses a fast Fourier transform (FFT) algorithm.

To visualize whether the response would experimentally be observable, we compute from the DFT the ratio between the harmonic we want to study and the principal frequency. If the harmonic response is less than one percent of the principal response (i.e. 40 dB in amplitude ratio), the harmonic is deemed not observable[11]. For simulations with a subharmonic ratio that is larger than 1, the oscillation is deemed non-physical. These ratios will be visualized in contour plots in the results section.

Lastly, we have to look at the maximum radius of the bubble in each oscillation. Because there are no limitations on the bubble radius in our model, the radius could theoretical ex-

[11]This tolerance level is due to the resolution of the measuring equipment used in experiments. The level depends on the type of equipment used, but we assume here that level to be 1 percent of the principal frequency[27].

pand to very large diameters without bursting. This is, however, not physically possible in experiments. For this reason we set a maximum radius for the microbubble, after which the results are deemed non-physical because in reality the bubble would have already burst. The maximum radius is set to $1.6 \cdot a_0$, with a_0 the initial radius of the bubble, which is in practice for hard-shell bubbles such as Sonovue beyond the point of structural failure.

3.5 Validation of chosen method

Before calculating with our modified model the bubble dynamics in the vicinity of the capillary walls, we first try to validate our differential equation and the simulation code for cases that have been experimentally validated. First, we test whether we get the expected results of the Rayleigh-Plesset equation back, when we let the diameter D and length L of the tube go to infinity. Secondly, we reproduce the results that were published for the same model in the paper by Qamar et al. [11], and compare them.

Validation of the model for an infinitely large tube

One test to see if the model can be interpreted properly, is by showing it diverges back to the Rayleigh-Plesset equation for oscillations in free-water, if one takes large D and L for the dimensions of the tube. Although, this validation has been implied by Qamar et al. [11], we will explicitely reproduce this. The validation can be done in two ways. One approach is the algebraic solution, whereby the starting point is equation (3.14) and letting D and L go to infinity. Then with the correct mass conservation and boundary conditions it is to be expected that we get the Rayleigh-Plesset equation back.
Another approach is by simulating equation (3.14) for large D and L and comparing it to the simulation program of Hoff. Sadly, because of the aforementioned MATLAB solver, the simulation fails for large D and L. This is why we can only do the first approach.

To show that our differential equation will diverge to the Rayleigh-Plesset equation, we will have to look at our equations:

$$\underbrace{\int_{a(t)}^{L/2} \left(\frac{\partial u}{\partial t}\right) dx}_{\text{Unsteady inertia term (1)}} + \underbrace{\frac{1}{2}\left(u_{L/2}^2 - u_a^2\right)}_{\text{Steady inertia term (2)}} + \underbrace{\frac{H_L}{\rho}}_{\text{Head Loss (3)}} = \underbrace{\frac{p_a - p_{L/2}}{\rho}}_{\text{Pressure (4)}}, \tag{3.23}$$

$$\underbrace{\frac{16}{\beta D^2}\left[\frac{L}{2} - a\right]\left[a^2\ddot{a} + 2a\dot{a}^2\right] + \dot{a}^2}_{(1)} + \underbrace{\frac{1}{2}\left(\frac{1028\, a^4 \dot{a}^2}{\beta^2\, D^4} - \dot{a}^2\right)}_{(2)}$$
$$+ \underbrace{\frac{512 \mu_L a^2}{\beta \rho D^4} \dot{a}\left[\frac{L}{2} - a\right]}_{(3)} = \underbrace{\frac{p_a - p_{L/2}}{\rho}}_{(4)}. \tag{3.24}$$

Now we will see what happens if we let D and L go to infinity.

First we will look at term (3) in the equations. Both D and L go to infinity, but because of the D^4 in the denominator, that part will dominate and thus the head loss will go to zero. Term (4) will stay the same, but instead of $p_{L/2}$ it will change to the pressure at infinity p_∞. In term (2) we have to find a new expression for u_∞ when integrating to infinity. A boundary condition for this system with boundaries at infinity is that the velocity there has to go to zero. Thus this part in term (2) will drop out. This is also confirmed because for large D the term D^4 in the denominator will let the velocity at the boundary of the system go to zero.

To correctly change term (1) to our new system we have to change the mass conservation we used to one that is correct in an infinite fluid domain. Let start again with the integration of term (1), and again apply the Leibniz integration rule [18]:

$$\int_{a(t)}^{\infty} \left(\frac{\partial u}{\partial t} \right) dx = \frac{\partial}{\partial t} \int_{a(t)}^{\infty} u \, dx + \dot{a}^2 \tag{3.25}$$

Because D and L both go to infinity, our system has become spherically symmetric in its oscillations. Now our integration along the centerline of the tube is equal to an integration along a radial streamline. Then the integral on the right-hand side becomes:

$$\frac{\partial}{\partial t} \int_{a(t)}^{\infty} u \, dx = \frac{\partial}{\partial t} \int_{a(t)}^{\infty} u \, dr. \tag{3.26}$$

From this point on our problem becomes equivalent to the one in section 2.3 where we have derived the Rayleigh-Plesset equation.

$$a\ddot{a} + \frac{3}{2}\dot{a}^2 = \frac{p_a - p_\infty}{\rho} \tag{3.27}$$

In the end we see that we indeed get the Rayleigh-Plesset equation back when taking the dimensions of the tube to infinity.

Comparison to the article

To make sure we are simulation our model correctly, we reproduce some results of this same model tested in the paper by Qamar et. al. [11]. Here, we aren't looking for exactly the same data in the figures, but for similiar responses of the microbubbles. This, because Qamar et al. used a different type of shell model[12].

In figures 3.4 and 3.5 we see on the left the figures from the paper, and on the right our own figures. For both figures we see a similar relation between the paper and our own data. Our own microbubbles seem to be more damped because the maximum radii are everywhere lower compared to the maximum radii of the paper's microbubbles. This might be because of the different shell models that are used in the calculation of these figures.

[12]The type of shell model is not clearly stated in the article, but the data is compared to experimental data of microbubbles with a certain type of lipid monolayer as shell [32].

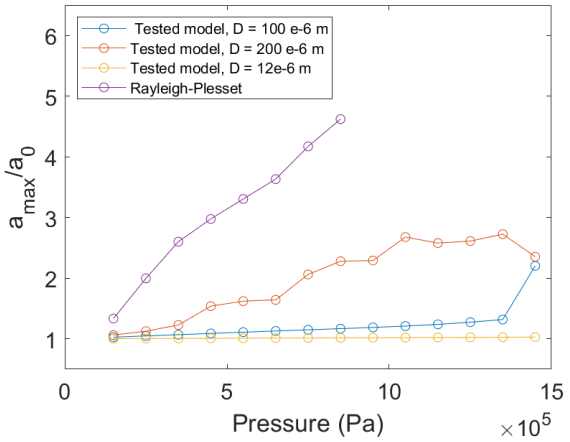

(a) Own simulated data

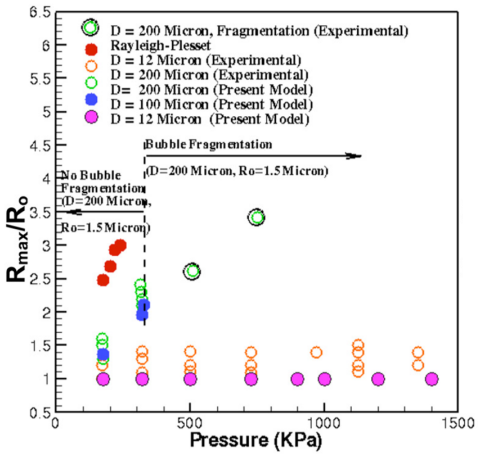

(b) Graph from paper by Qamar et al.[13]

Figure 3.4: a) The change in the maximum radius simulated for 3 different tube diameters, compared to the Rayleigh-Plesset equation. Here, $a_0 = 1.5$ micron, with a driving frequency of 2.25 MHz. This graph is meant to be compared with figure b) by Qamar et al., see [11] (with the same parameters). In their graph are both experimental and numerical data plotted to be compared with the Rayleigh-Plesset model in red. R_0 and a_0 are both the initial radius of the bubble. R_{max} and a_{max} are both the maximum radius of of the entire oscillation.

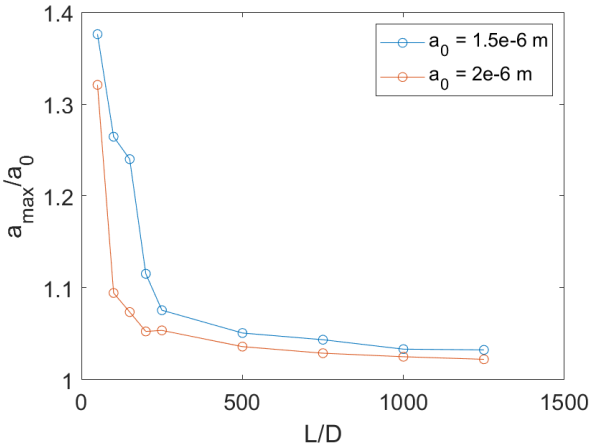

(a) Own simulated data

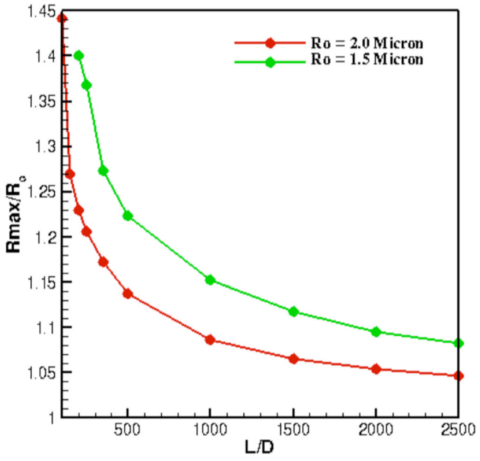

(b) Graph from paper by Qamar et al.[14]

Figure 3.5: a) The change in the maximum radius simulated for 2 different microbubble radii for different ratios of L and D. In these ratios, D is fixed at 200 micron and L changes in size. The driving frequency is 2.25 MHz, the PNP is 175 kPa. This graph is meant to be compared with figure b) by Qamar et al., see [11] (with the same parameters). R_0 and a_0 are both the initial radius of the bubble. R_{max} and a_{max} are both the maximum radius of of the entire oscillation.

[13]Reprinted from [Qamar, Adnan et al. "Dynamics of micro-bubble sonication inside a phantom vessel." *Applied physics letters* vol. 102,1 (2013): 13702. doi:10.1063/1.4773909], with the permission of AIP Publishing.

[14]ibid.

4 Results and Discussions

The results in this section will be separated into three parts. First, we will look at the influence of viscosity on on the harmonic responses of the oscillating microbubble. This will be simulated with the Rayleigh-Plesset equation, to see if we can validate some experimental findings with an existing and widely used model. Secondly, we will look at the effects of a rigid tube on the harmonic responses of an oscillating microbubble. In this section we will keep the viscosity equal to the viscosity of water, $\mu_L = 1.0$ mPas. In the last part, we will take some of the results and compare them directly to experimental data. Each result section is followed by a discussion of those results.

In the results, we will use contour plots to visualize the (sub/ultra)harmonic responses of the microbubble. As explained in more detail in section 3.4, this is done by determining the ratio between the principal frequency and the (sub/ultra)harmonic in question. All the contour plots shown in the result sections will have the same color scale and thus can be compared with each other. Figure 4.1 is an example of such a contour plot.

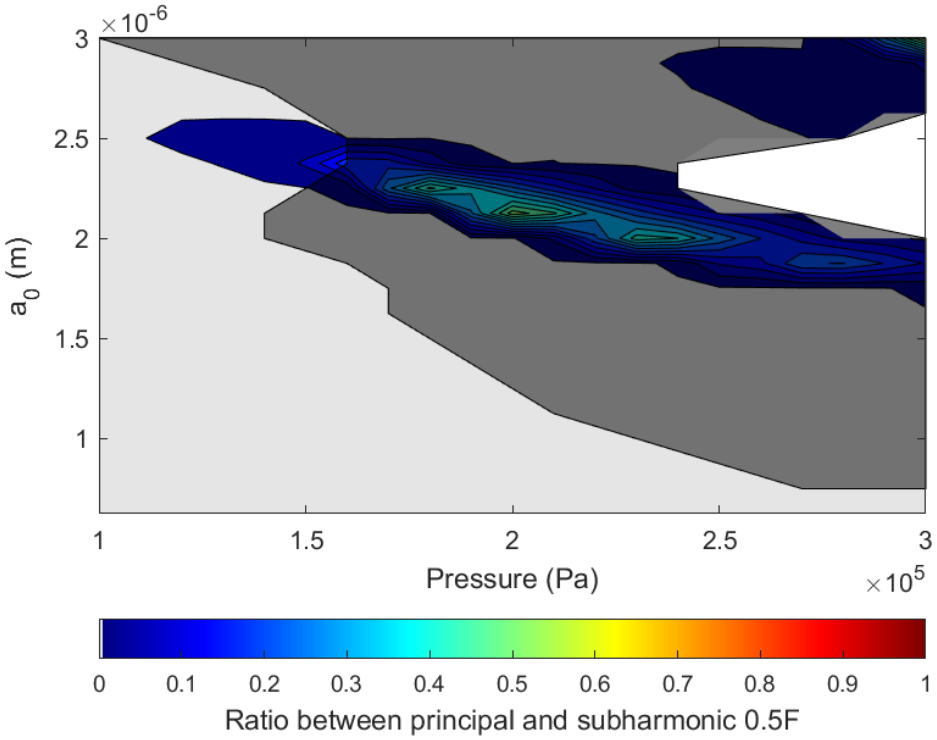

Figure 4.1: A contour plot of the subharmonic frequency response of a microbubble in a fluid with viscosity $\mu_L = 0.7$ mPas, simulated with the Rayleigh-Plesset equations. The response is simulated for a range of initial bubble radii a_0 and peak negative pressures. The gray area is where the response is less than 1 percent of the response of the principal frequency at 1MHz. The white area is where the simulation failed due to calculation restrictions by MATLAB.

In figure 4.1 we see the subharmonic response of a microbubble in a infinite domain of fluid. This result was simulated with the Rayleigh-Plesset equation. In the figure we see a range of microbubble radii a_0, chosen according to the bubble distribution of Sonovue (see figure 3.3 in section 3.4), against a range of pressures. The colored areas indicate the subharmonic response with a ratio larger than 0.01, with the scale of the colors given in the colorbar on the bottom of the figure. The gray areas indicate a subharmonic response of less than 0.01 and is determined to be not detectable as explained in section 3.4. The white areas are the simulations that failed due to calculation restrictions of MATLAB in which we simulated all our results. The white areas also indicate where the model becomes non-physical, due to a subharmonic response ratio that is larger than 1. The darker shaded area, outlined with a black line, is the area where the microbubbles would have burst because of there large radius.

Considering all this, the only physical part in this figure, where we expect a subharmonic response, is for bubbles of a radius around 2.5 micron with pressures between $110 - 160$ kPa.

4.1 Results for viscosity

4.1.1 Effects on harmonics responses

A first observation is that there are no grey areas in the first harmonic responses. This means that for the entire region that can be interpret as physical, there is a first harmonic response detectable. The largest harmonic response for all viscosities is around a bubble radius of 2.5 micron. Although, this response subdues for higher fluid viscosities, the location of this larger harmonic response does not shift, and thus only changes in magnitude.

The dark shaded area, which represents microbubbles that have already burst, does not change much for different viscosities and seems to have a slanting direction from the upper left to the bottom right. There is a small indentation in this line around the maximum harmonic response.

4.1.2 Effects on sub- and ultraharmonics responses

We observe immediately a difference between the harmonics in figure 4.2 and the subharmonics in figure 4.3. There is only a small region in the subharmonic contour plots where the subharmonics are experimentally observable. For all viscosities, almost the whole plot is grey except for a small oblique region that starts for bubble radii around 2.5 micron. This is around the same spot where we saw the maximum magnitude of first harmonic responses in figure 4.2. As with the harmonic response, the subharmonics seem to diminish for higher viscosities.

In figure 4.4 we see the ultraharmonics response from the oscillating microbubbles. These figures are in orientation similar to the subharmonic contour plots, but the magnitude of the ultraharmonics are lower than the subharmonics. For fluid viscosities above $\mu = 1.3$ mPas, there are no detectable ultraharmonics left.

4.2 Discussion of viscosity effects

Considering the change of all the (sub/ultra)harmonics with changing viscosity, we observe the intuitively expected resonance behavior of the bubbles: The viscosity is a damping term for the oscillation of the microbubble. The larger the viscosity is, the more it dampens the oscillation. As a consequence, it will also have a damping effect on the frequency responses of the microbubble. It does not change the profile of the contour plots we saw, and only effect the magnitude of the responses.
It is however to be noted that in the Rayleigh-Plesset equation, the viscosity of the liquid is only taken into account in close proximity of the bubble-fluid interface. In general, the fluid is considered as inviscid. This might imply that the damping due to viscosity will be larger in experimental set ups than this model shows. For *in vivo* experiments, with blood being a more viscous fluid than water, these results might already explain why in some ranges there are no subharmonic or ultraharmonic reponses, without simulation a tube around the oscillating bubble.
Also, we have to keep in mind that not all microbubble radii are of the same importance to the total signal. For Sonovue, there are more microbubbles radii in the range of $0.75-1.5$ micron, then larger microbubbles. Thus, a sub- or ultraharmonic response in larger microbubble sizes does not immediately mean that you will see this response in experiments.

The concentrated areas with large harmonic responses in figure 4.2 can be explained with the resonance frequency of the microbubbles. Depending on the size and characteristics of the microbubble, each bubble has its own natural frequency. When a microbubble is driven near this frequency, resonance occurs and the harmonic response grows. It also seems that the sub- and ultraharmonic responses occur in regions of the contour plot with the bubble radii that are driven near their natural frequency. This, however, should be comfirmed by also changing the frequency of the acoustic source and observe the change in the responses of the microbubble.

4.3 Results for rigid tube effects

The simulations for this section were done for every possible combinations of parameter in tube dimensions and microbubble sizes, describe in section 3.4. This, however, is to much data to show in this section, and thus a selection was made. The data concerning the change in harmonic response due to change in tube length will not be discussed, because there was hardly any observable change in the response. Also, all these simulations were calculation for the same viscosity, $\mu = 1.0$ mPas, because of the computation time needed to get all this data.

4.3.1 Effects on harmonics responses

In figure 4.5 we see the harmonic response for an oscillating microbubble inside a rigid tube. It shows the response for different types of tube diameters. The tube length is fixed at 150 micron and the fluid viscosity is fixed at 1.0 mPas.
First of all, we see in these plots a large portion of the model that is considered non-physical, indicated with white. These are the parts where the subharmonic response grows larger than

the principal frequency. Only for the smaller microbubbles can we look at the harmonic response of the microbubbles.

The shape of the harmonic response is very similar to the one we saw in figure 4.2, only more flattened and directed towards the smaller bubble sizes. Again we see a specific area with a larger harmonic response, now around a bubble radius of 1 micron. As the diameter of the tube grows larger, the whole figure seems to shift slightly upwards. Where in figure 4.5.a this area is around 1 micron, for figure 4.5.f it has shifted towards approximately a radius of 1.5 micron. Similarly, as was observed in figure 4.2, the maximum radius line within the figure makes a small indentation around the area where the response is largest. Though, for radii larger than approximately 1.5 micron (dependent of the tube diameter), the shaded area on the contour plot does not follow the same pattern as with the Rayleigh-Plesset equation, and is more uneven across the whole figure.

4.3.2 Effects on sub- and ultraharmonics responses

In figure 4.6 we see the subharmonic response of an oscillating microbubble inside a tube. It shows the response for different types of tube diameters, with a fixed tube length at 150 micron and the fluid viscosity is fixed at 1.0 mPas.

Here, we have the same white and shaded area as we observed in figure 4.5, but the subharmonic response is very different from the harmonic response. It seems as though we can recognize the shape from the Rayleigh-Plesset response in this figure (see figure 4.3). Again, it looks like a flattened version of the Rayleigh-Plesset response, up untill a microbubble radius around $1 - 1.5$ micron (dependent on the tube diameter). Above this it rapidly goes to non-physical areas.
What is new here, and what we do not see in the Rayleigh-Plesset response, is a sudden quick growing subharmonic response as an oblique line across our contour plot. There, the growth in subharmonic response seems to have a steep slope and switches quickly from physical to non-physical.

The ultraharmonic response of figure 4.7 is similar to the orientation of the subharmonic response, but again the magnitude of the response is lower. For instance, we see a less steep change in magnitude on the transition from physical to non-physical regions.

4.4 Discussion of rigid tube effects

When we look at the change in sub- and ultraharmonic responses for an oscillating microbubble in a rigid tube, it is good to first compare it the Rayleigh-Plesset results. If we compare the figures for a visocity of $\mu = 1.0$ mPas, on a first glance the figures look very different. But if you were to flatten the Rayleigh-Plesset figures and shift them to the right, it resembles the parts of the figures we have for a rigid tube. Whithin this shift, we thus see that the natural frequency changes for microbubbles that are oscillating in a rigid tube. This result agrees with other papers that studied this phenomenon. The smaller the vessel, the more it lowers the natural frequency of the microbubble [33][34]. Combining these results, we see

that the sub- and ultraharmonics do not seem to dissappear in a tube but more likely shift to different bubble sizes and pressures. This might be explained due to the fact that larger microbubbles in a tube are more dampened than smaller ones.

The large non-physical area in the contour plots is a new phenomenon we do not see in the Rayleigh-Plesset figure. In reality these microbubbles might not exist in these regions because of the steep slope in the subharmonic response. In those transitions the microbubble suddenly and very quickly starts to change its oscillation, and might burst because of this. These area might thus indicate where inertial cavitation takes place. It would be interesting to investigate whether sub- and ultraharmonics are a sign of the onset on inertial cavitation. Also, for the smaller microbubbles we see that this region is under the dark shaded area, where these microbubbles do not exist anymore. More experimental work should be done in these regions to make sure there isn't something else going on, and whether it is just the model that is breaking down.

4.5 Comparison to experimental results

In figure 4.8, we compare some experimental data [10] with the frequency responses of a microbubble inside a 12 micron diameter and 150 micron length tube. In the figures 4.8.a, 4.8.b and 4.8.c, the viscosity of the fluid is 1.6 mPas, representing the viscosity of blood plasma. The range of microbubble sizes is in this figure smaller than the other figures in the results section. This, because we only want to look at the bubble radii that are most frequently present in the contrast agent Sonovue (see figure 3.3 in section 3.4). No color bar was added to this figure due to lack of space, but the color scale is the same as all the other contour plots. The sub figure 4.8.d is the *in vivo* experimental data for a bolus of Sonovue sonicated with a pressure of 400 kPa PNP an frequency 1 MHz, with frequency on the x-axis and on the y-axis the amplitude in dB.

We see in figure 4.8.d that there are no sub- or ultraharmonics detected. When we look at 400 kPa in the contour plots in this figure, there are also no sub- or ultraharmonics present. However, these contour plots do indicate that no microbubbles can be present at 400 kPa, because they have already burst. But in the experimental data, it was shown that there are still microbubbles present that scatter the other harmonics seen in that figure.

4.6 Discussion of comparison with experimental results

In figure 4.8 we compare some experimental data with the numerical model we have created. It is interesting to see that our model correctly predicts that there are no ultraharmonics or subharmonics at an insonication of 400 kPa, as is confirmed with the experimental data in figure 4.8. There are, however, some differences that we can observe. The most important one is, that our numerical model predict that no microbubbles are left at a pressure of 400 kPa. This is an incorrect prediction, as can be seen in the experimental data. There, they still see a rise in the harmonic response at 400 kPa. From this we might be able to conclude that the maximum radius we set for the microbubbles is incorrect. It might be the case that this maximum radius differs per initial microbubble radii, and that it also differs depending

on the way the microbubble oscillates. Then, if the black shaded area is in reality smaller, we might be able to detect sub- and ultraharmonics at a pressure of 300 kPa (where our numerical model predict the sub- and utraharmonics exist).

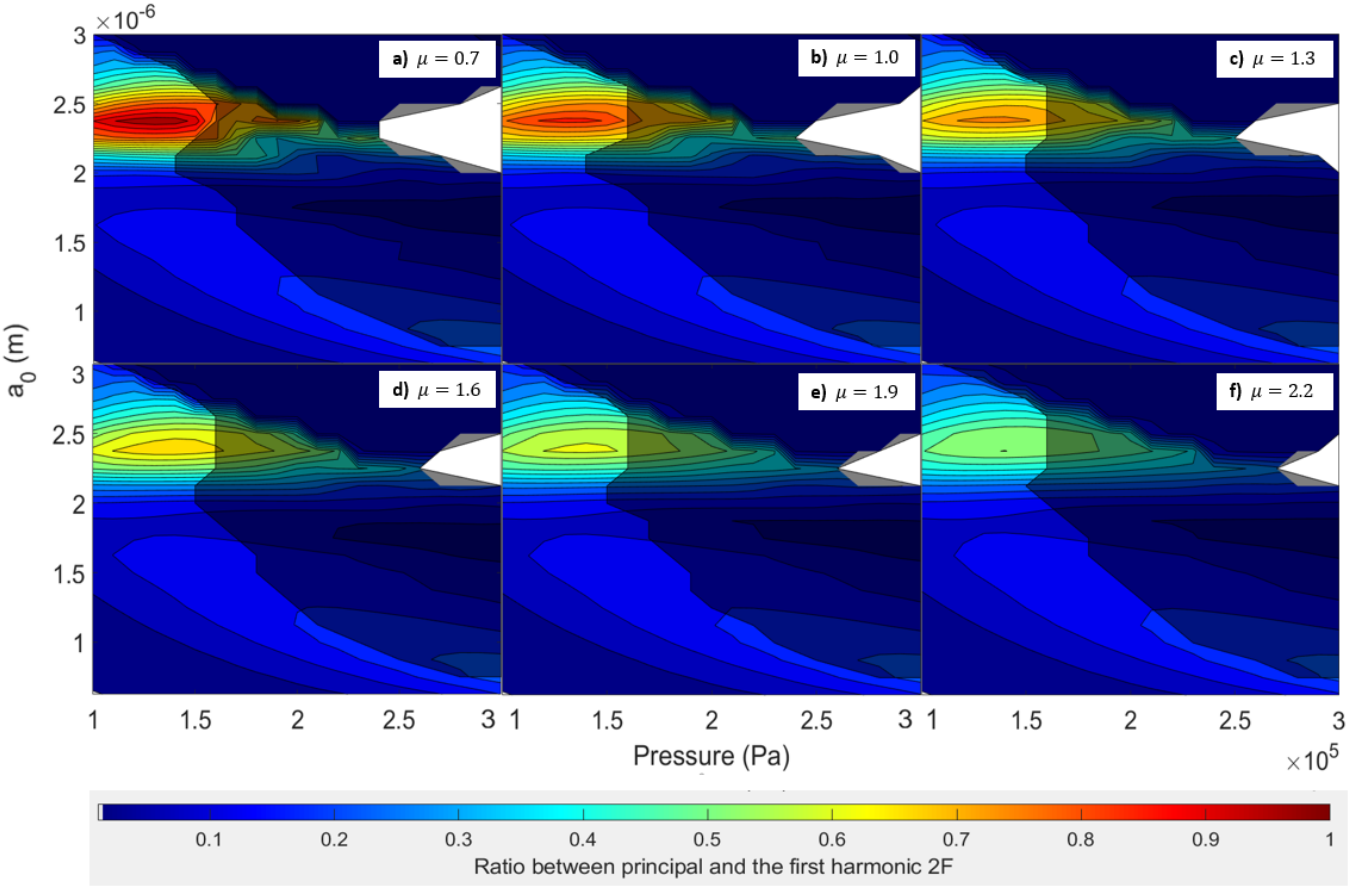

Figure 4.2: The harmonic response of a microbubble simulated with the Rayleigh-Plesset equation for different type of fluid viscosities. The response is given as the ratio between the first harmonic frequency and the principal frequency. All viscosities are given in mPas. The grey area is where the response is less than 1 percent of the response of the principal frequency, at 1 MHz. The white area indicates where the simulation failed due to calculation restrictions by MATLAB. The parts that are shaded transparent black, are the oscillations where the bubble radius becomes to large to be physically possible; $(1.6 \cdot a_0)$. In these regions the bubble wouldn't exist anymore.

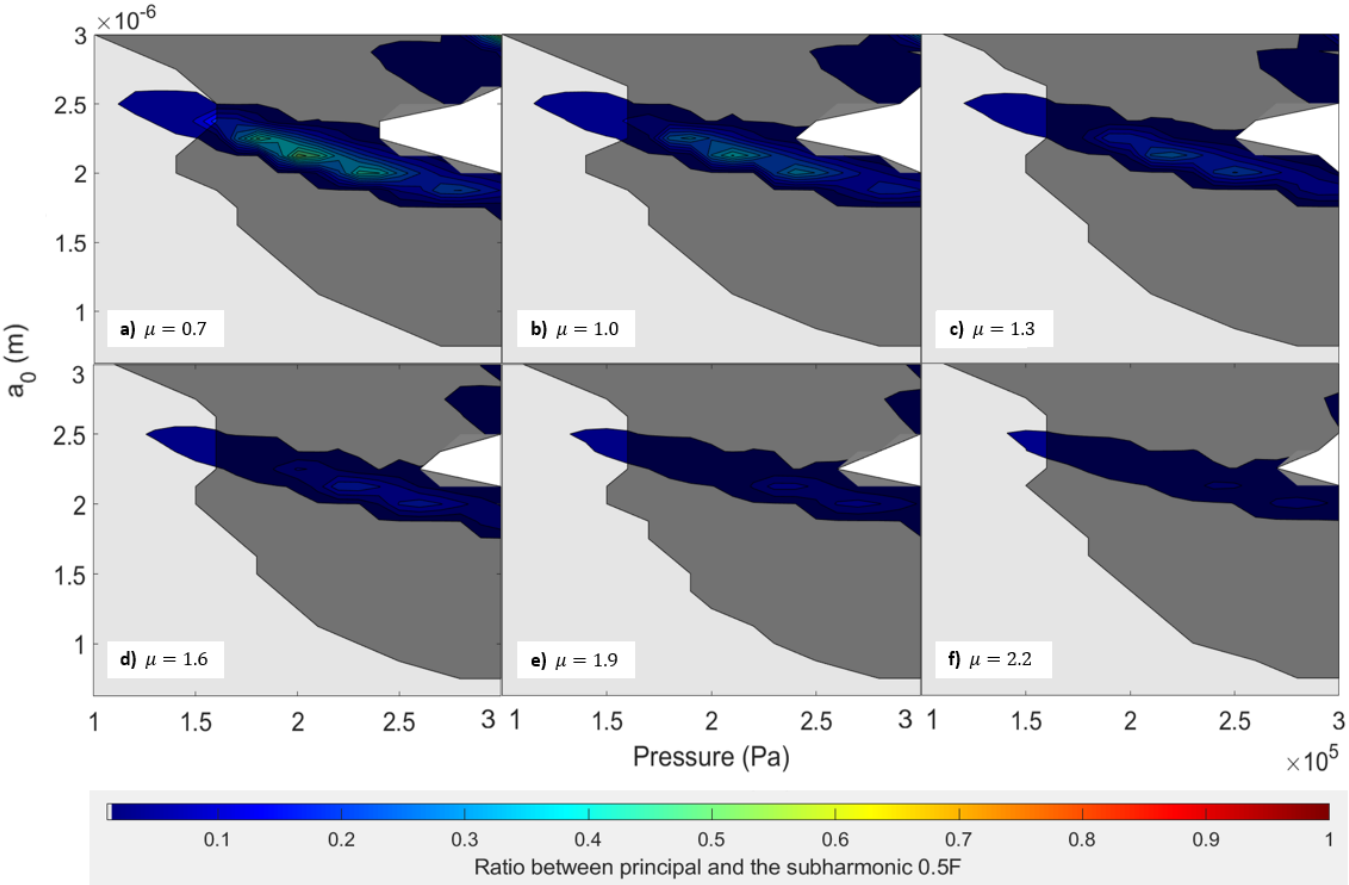

Figure 4.3: Subharmonic response of a microbubble simulated with the Rayleigh-Plesset equation for different type of fluid viscosities. The response is given as the ratio between the subharmonic frequency and the principal frequency. All viscosities are given in mPas. The grey area is where the response is less than 1 percent of the response of the principal frequency, at 1 MHz. The white area indicates where the simulation failed due to calculation restrictions by MATLAB. The parts that are shaded transparent black, are the oscillations where the bubble radius becomes to large to be physically possible; $(1.6 \cdot a_0)$. In these regions the bubble wouldn't exist anymore.

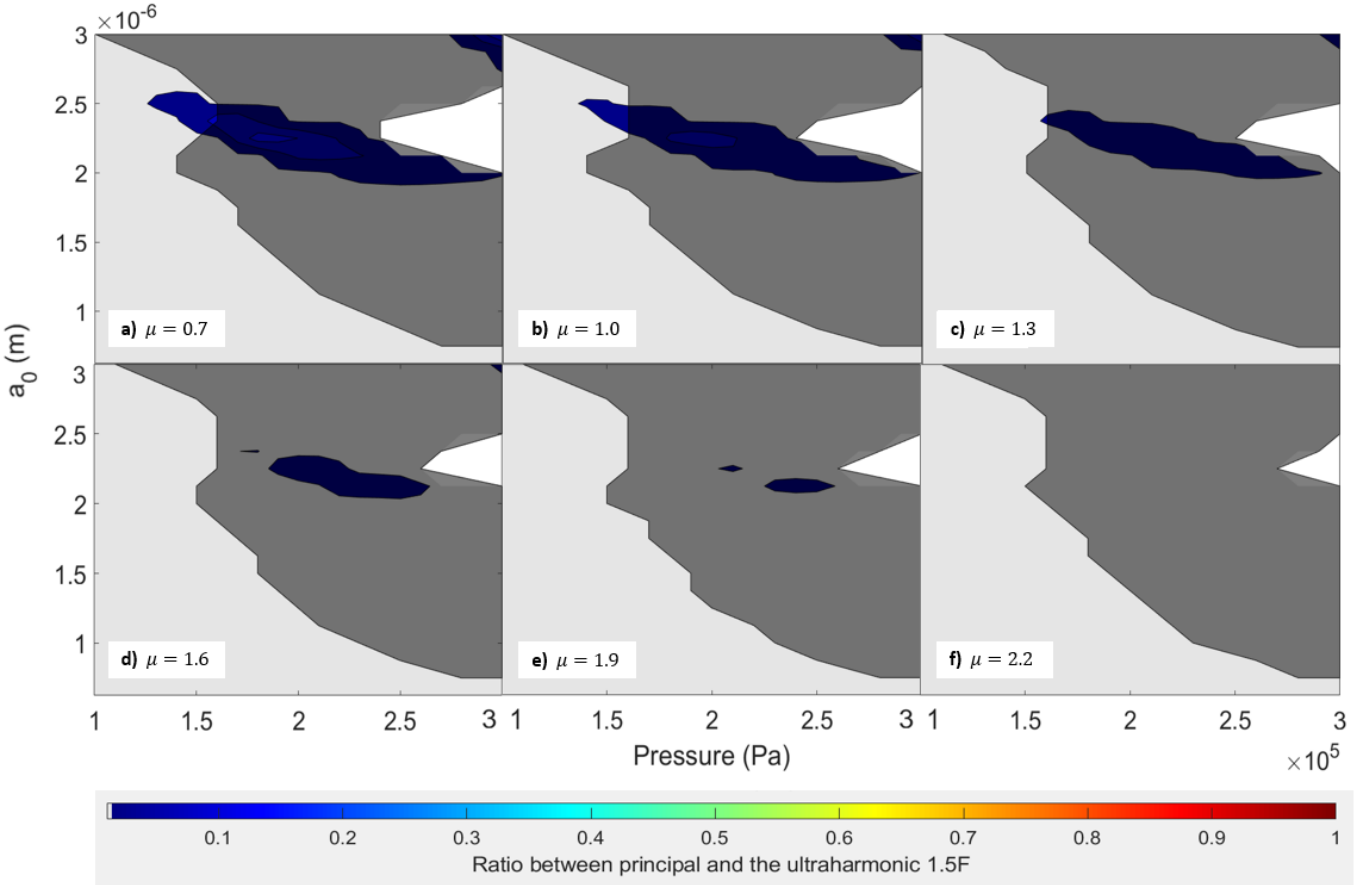

Figure 4.4: First ultraharmonic response of a microbubble simulated with the Rayleigh-Plesset equation for different type of fluid viscosities. The response is given as the ratio between the first ultraharmonic frequency and the principal frequency. All viscosities are given in mPas. The grey area is where the response is less than 1 percent of the response of the principal frequency, at 1 MHz. The white area indicates where the simulation failed due to calculation restrictions by MATLAB. The parts that are shaded transparent black, are the oscillations where the bubble radius becomes to large to be physically possible; $(1.6 \cdot a_0)$. In these regions the bubble wouldn't exist anymore.

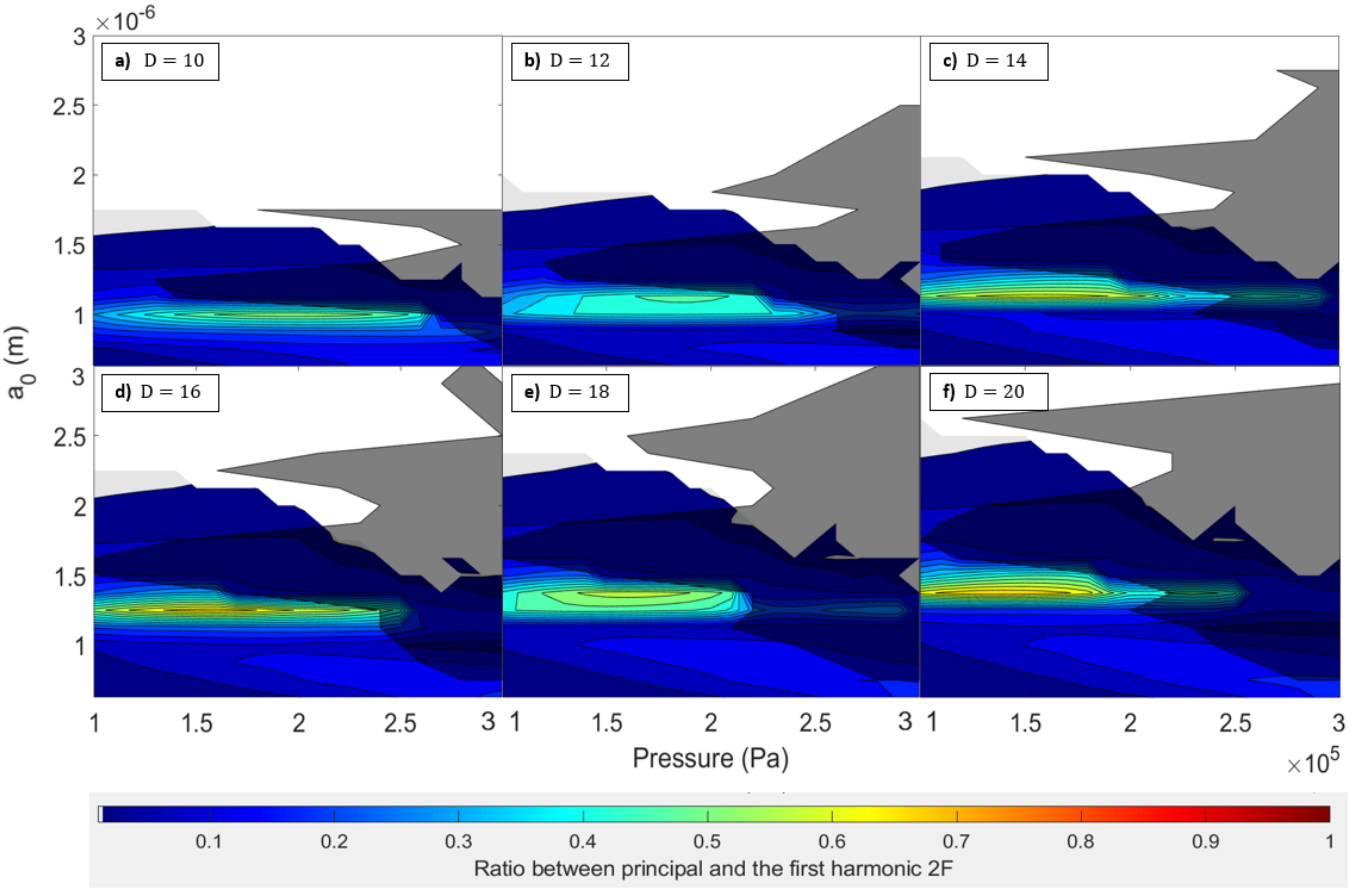

Figure 4.5: The first harmonic response of a microbubble simulated with the new model for different type of tube diameters. The response is given as the ratio between the first harmonic frequency and the principal frequency. All diameters are given in micron. The grey area is where the response is less than 1 percent of the response of the principal frequency, at 1 MHz. The white area indicates where the simulation failed due to calculation restrictions by MATLAB, or due to non-physical results. The parts that are shaded transparent black, are the oscillations where the bubble radius becomes to large to be physically possible; $(1.6 \cdot a_0)$. In these regions the bubble wouldn't exist anymore. The length of the tube is fixed at 150 micron.

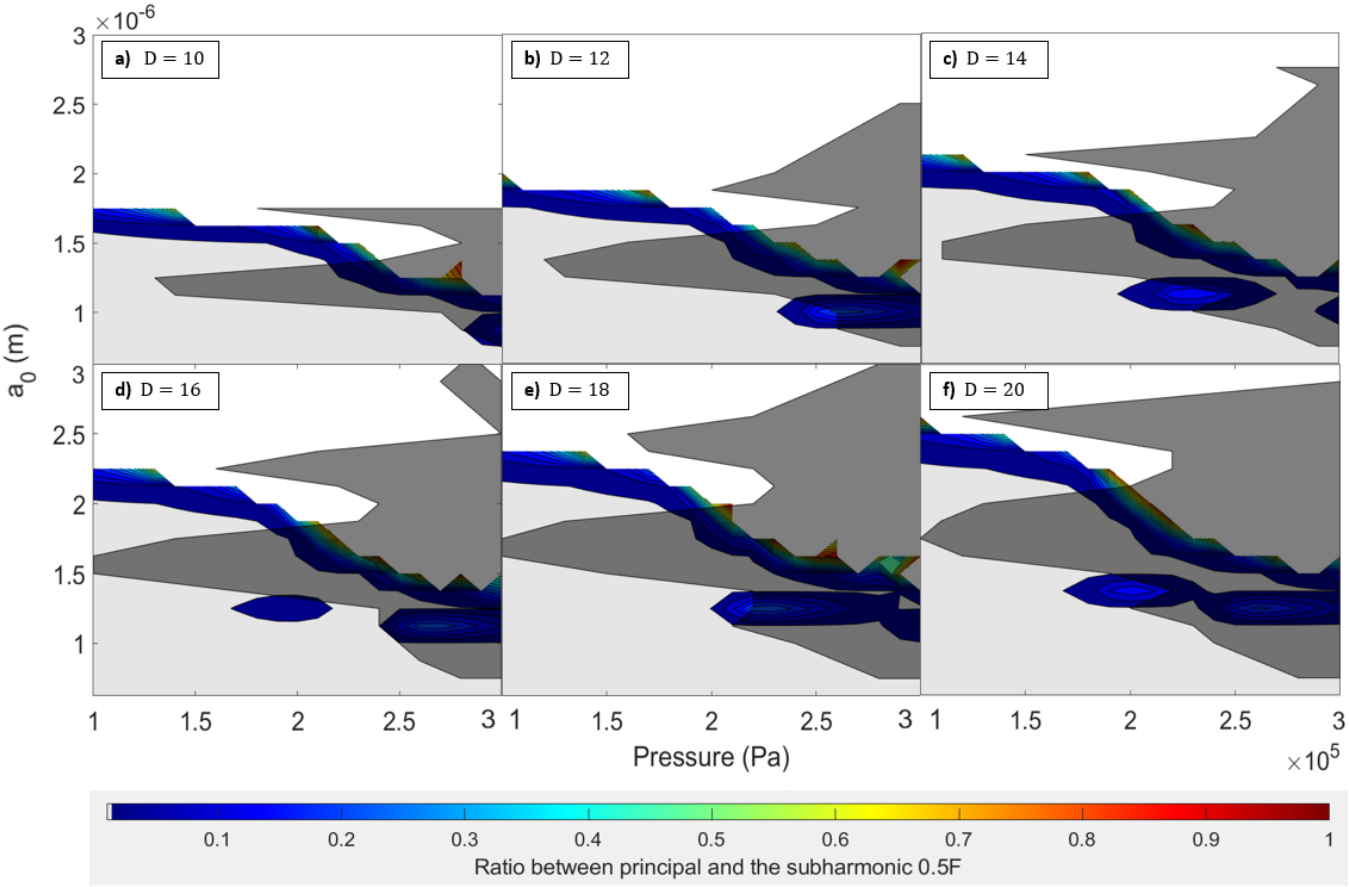

Figure 4.6: The subharmonic response of a microbubble simulated with the new model for different type of tube diameters. The response is given as the ratio between the subharmonic frequency and the principal frequency. All diameters are given in micron. The grey area is where the response is less than 1 percent of the response of the principal frequency, at 1 MHz. The white area indicates where the simulation failed due to calculation restrictions by MATLAB, or due to non-physical results. The parts that are shaded transparent black, are the oscillations where the bubble radius becomes to large to be physically possible; $(1.6 \cdot a_0)$. In these regions the bubble wouldn't exist anymore. The length of the tube is fixed at 150 micron.

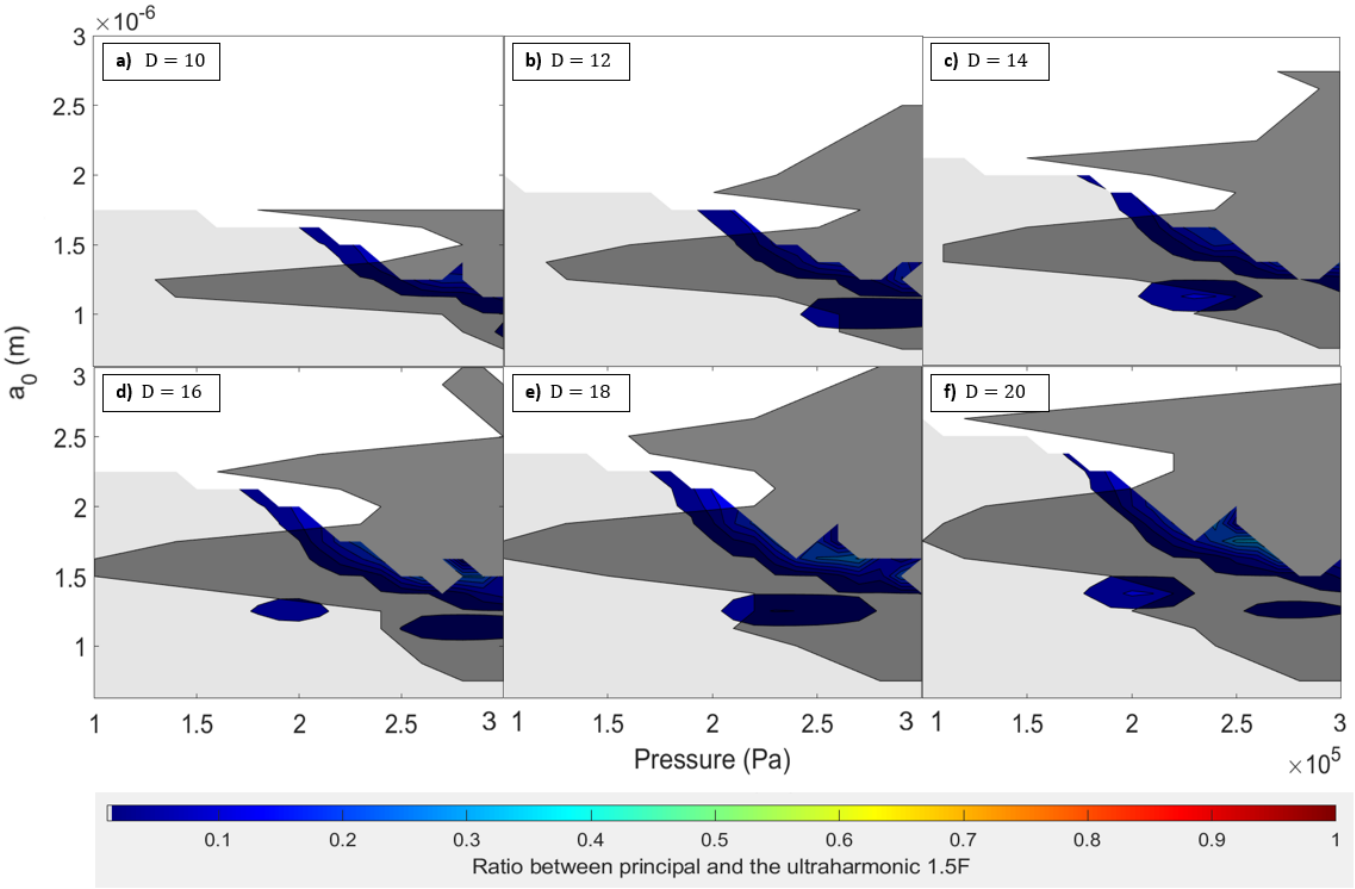

Figure 4.7: The first ultraharmonic response of a microbubble simulated with the new model for different type of tube diameters. The response is given as the ratio between the first ultraharmonic frequency and the principal frequency. All diameters are given in micron. The grey area is where the response is less than 1 percent of the response of the principal frequency, at 1 MHz. The white area indicates where the simulation failed due to calculation restrictions by MATLAB, or due to non-physical results. The parts that are shaded transparent black, are the oscillations where the bubble radius becomes to large to be physically possible; $(1.6 \cdot a_0)$. In these regions the bubble wouldn't exist anymore. The length of the tube is fixed at 150 micron.

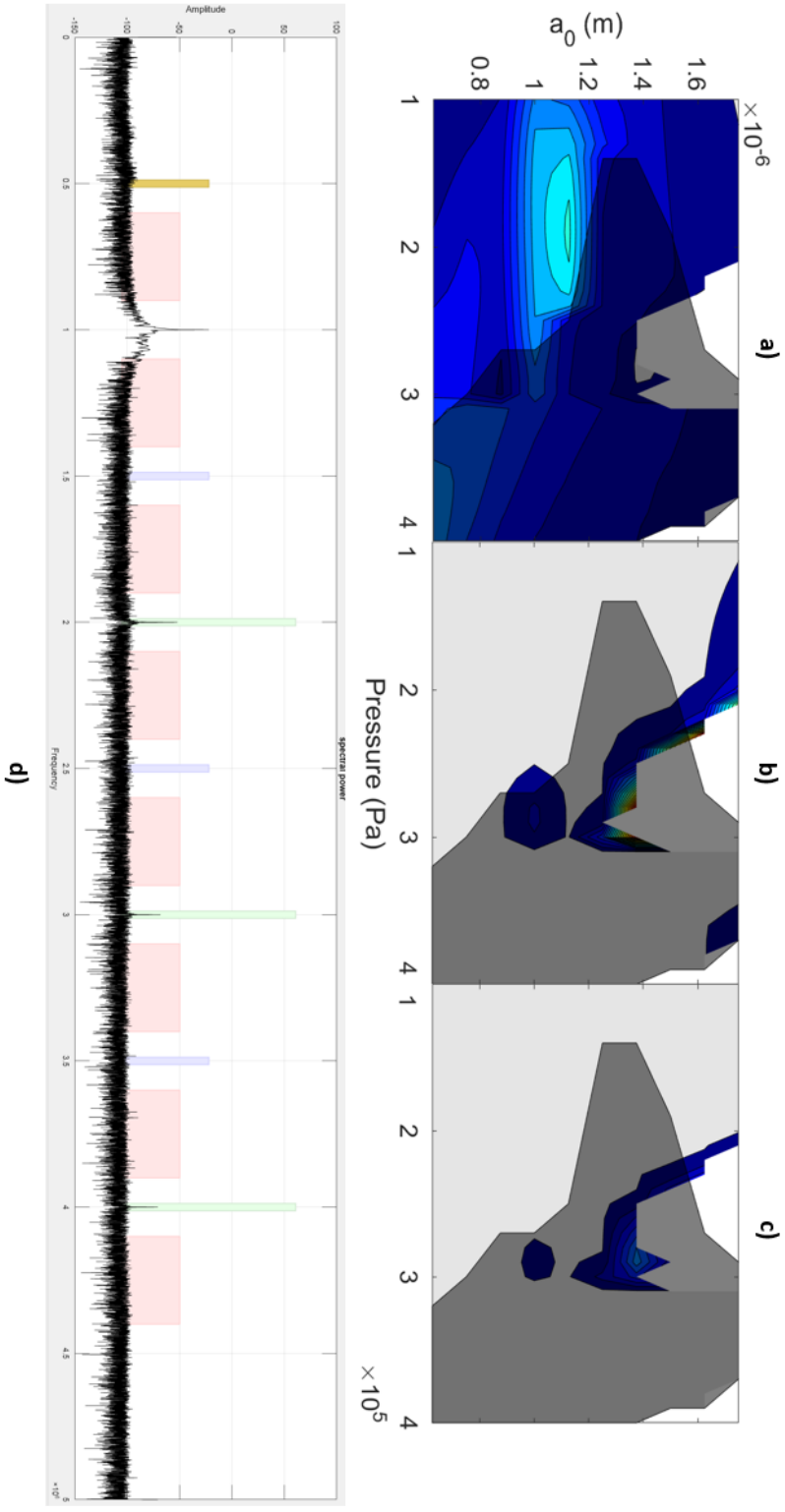

Figure 4.8: A comparison between the numerical model and *in vivo* results. Sub figures **a)**, **b)** and **c)** are the simulation of a range of microbubble sizes a_0 inside a rigid tube of length $L = 150$ micron and diameter $D = 12$ micron. The fluid viscosity is that of bloodplasma, 1.6 mPas. Figure **a)** shows the first harmonic, figure **b)** shows the subharmonic and figure **c)** shows the first ultraharmonic. All these sub figures were driven at a frequency of 1 MHz. Sub figure **d)** shows the insonication of a bolus of Sonovue contrast agent inside a mouse brain, sonicated with a frequency of 1 MHz and a pressure of 400 kPa PNP (from [10]). On the x-axis we see the frequency, with the harmonics indicated with green, the subharmonic with yellow and the ultraharmonic with purple. The y-axis gives the amplitude in dB.

4.7 General discussion of used model

In this section we will give some general remarks on the model and the assumptions and approximations that were made to get to our end results.

There were numerous of assumptions made to establish our model, which oversimplify the considerably more complex real situation. Potentially one of the most important ones, is that we assume a spherically symmetric oscillation of the bubble. In section 3 we already underlined that this assumption is actually not a good one for small capillary vessels. The consequences of this assumption is that the we over estimate the maximum radius in the direction of the vessel walls. This might also be an explanation for the differences we saw between experimental data and our model in the region where the microbubbles still exist or not (see section 4.6). Also, a non-symmetric microbubble oscillation might also effect the sub- and ultraharmonic response.

Another assumption is that the insonication on the microbubble is at the end of the tube. This is not realistic in experimental and clinical set ups, where the microbubbles are sonicated outside the body. Because of this, the orientation between the vessel and the acoustic source can be different for every capillary. And if the microbubble is sonicated from different directions, the fluid flow inside the vessels near the microbubble might be effected differently. The assumption of laminar flow might become unjust because of this.

In this model, we only determine the frequency domain of the oscillation of the microbubble. This is, however, not what is measured in experiments. The scattered pressure that the microbubble radiates is measured and converted into a frequency domain. The scattered pressure decreases in magnitude by the tissues it as to pass through before it arrives at the detection equipment. This means, that even if our models predicts small sub- and ultraharmonic responses, they might not be detectable once arrived at the detector.

A last important approximation that we made, is the model itself. The way we added Poisseuille flow to the Rayleigh-Plesset equation was, given the complexity of the system, somewhat oversimplified. It would have been better to solve the entire Navier-Stokes equations of course, though these would have been more difficult to solve numerically. In the second paper by Qamar et al. [24], they improved the model by not adding a constant head loss, but making the head loss term a function of the induced wall shear stresses by the fluid. This model followed the experimental data with which they compared their model to, a bit better than their first model.

Even though, there are a lot of parts in this model that are not exactly accurate compared to experimental data, it does give us an impression of the fundamental impact of the wall interaction of a capillary on the oscillation of a microbubble, and thus its frequency responses.

5 Conclusions and outlook

In this thesis we theoretically investigated the sub- and ultraharmonic response of a microbubble oscillating inside a rigid tube. We also analyzed the effects that change in viscosity can have on the sub- and ultraharmonic responses for a microbubble by means of numerical simulation of the Rayleigh-Plesset equation.

We observed that the magnitude of the sub- and ultraharmonic responses depends on the damping of the viscosity of the fluid, even when the viscosity is only taken into account near the bubble surface. Our results show that for viscosities higher than 1.3 mPas no ultraharmonics are predicted for a acoustic source with frequency 1 MHz and pressure range of $100 - 300$ kPa PNP. This prediction can potentially explain the disappearance of sub- and ultraharmonics in measurements obtained *in vivo*, but this should be more investigated by, for instance, changing the viscosity in the tube model we also investigated in this thesis.

In the tube model, we observed a shift in all the frequency responses, and did not see them disappear due to change in magnitude. This shift might also be the reason between the differences seen in *in vitro* and *in vivo* experiments.
An important observation in the results is that in both models, the sub- and ultraharmonic responses only appear in small regions of the investigated ranges. The first harmonic response however, is observable for almost the entire physical range of the contour plots. Imaging with sub- and ultraharmonics is thus not ideal because they are very specific to bubble size and pressure, and might be a sign of the onset of inertial cavitation in the tube model. This suggests to a conclusion that sub- and ultraharmonics shouldn't be used for diagnostic purposes, and only for therapeutic purposes when inertial cavitation is wanted.

However, this model that is proposed to predict the sub- and ultraharmonic microbubble responses, needs to be validated with dedicated experiments before far fetched conclusions can be drawn from the theoretical results. Of particular importance is hereby also an in-depth analysis of the so called 'non-physical' regions, which have not been accessible in the scope of the conducted numerical simulations.

Another step would be, of course, to include more into the model, to make it a more realistic simulation. Some first leads for such extended simulations could for example be non-symmetric simulation, or calculating the scattered pressure that the microbubble radiates. Further research could also look into the frequency dependency of the sub- and ultraharmonics in the system and make an average signal over all the microbubbles with the microbubble distribution of the contrast agent that is used.

6 Acknowledgements

First of all, I would like to thank both my supervisors Mario Ries and Joost de Graaf for their expert advice and guidance during my research project. Especially Mario Ries, who gave me an opportunity to work on a physics project that has medical applications. I am also grateful to everyone in the research group of the Prinses Maxima Centrum, who made working in a new environment a lot easier. Lastly, I want to thank my friends and family for all their support, especially Franca Majoor, who gave great advice when I needed it and who helped me with my writing skills.

References

[1] D. Khismatullin, *Gas microbubbles and their use in medicine*, pp. 231 – 289. 01 2005.

[2] P. J. Frinking, A. Bouakaz, J. Kirkhorn, F. J. T. Cate], and N. [de Jong], "Ultrasound contrast imaging: current and new potential methods," *Ultrasound in Medicine Biology*, vol. 26, no. 6, pp. 965 – 975, 2000.

[3] E. C. Unger, T. O. Matsunaga, T. McCreery, P. Schumann, R. Sweitzer, and R. Quigley, "Therapeutic applications of microbubbles," *European Journal of Radiology*, vol. 42, no. 2, pp. 160 – 168, 2002.

[4] T. Leslie and J. Kennedy, "High-intensity focused ultrasound principles, current uses, and potential for the future," *Ultrasound quarterly*, vol. 22, pp. 263–72, 01 2007.

[5] W. M. Pardridge, "Blood–brain barrier delivery," *Drug Discovery Today*, vol. 12, no. 1, pp. 54 – 61, 2007.

[6] M. Aryal, C. D. Arvanitis, P. M. Alexander, and N. McDannold, "Ultrasound-mediated blood–brain barrier disruption for targeted drug delivery in the central nervous system," *Advanced Drug Delivery Reviews*, vol. 72, pp. 94 – 109, 2014. Ultrasound triggered drug delivery.

[7] K. Yasui, ch. Acoustic cavitation and bubble dynamics. SpringerBriefs in molecular science, Ultrasound and sonochemistry, Cham: Springer, 2018.

[8] P. Shankar, P. Krishna, and V. Newhouse, "Advantages of subharmonic over second harmonic backscatter for contrast-to-tissue echo enhancement," *Ultrasound in Medicine Biology*, vol. 24, no. 3, pp. 395 – 399, 1998.

[9] A. M. Ivory, J. F. Meaney, A. J. Fagan, and J. E. Browne, "Optimisation of the transmit beam parameters for generation of subharmonic signals in native and altered populations of a commercial microbubble contrast agent sonovue®," *Physica Medica*, vol. 70, pp. 176 – 183, 2020.

[10] R. Haumann, E. 't Hart, M. P. P. Derieppe, H. C. Besse, G. J. L. Kaspers, E. Hoving, D. G. van Vuurden, E. Hulleman, and M. Ries, "A high-throughput image-guided stereotactic neuronavigation and focused ultrasound system for blood-brain barrier opening in rodents," *unpublished manuscript*.

[11] A. Qamar, R. Samtaney, and J. L. Bull, "Dynamics of micro-bubble sonication inside a phantom vessel," *Applied Physics Letters*, vol. 102, Jan 2013.

[12] P. K. Kunda, I. M. Cohen, and D. R. Dowling, *Fluid Mechanics*. Cambridge, Massachusetts: Academic Press, 6th ed., 2016.

[13] P. J. Pritchard, *Fox and McDonald's Introduction to Fluid Mechanics*. John Wiley sons, inc., 8th ed., 2011.

[14] Y. Nakayama and R. F. Boucher, *Introduction to fluid mechanics*. Oxford: Butterworth Heinemann, 1999.

[15] F. M. White, *Viscous fluid flow*. New York (N.Y.): McGraw-Hill Medical, 2nd ed., 1991.

[16] L. Hoff, *Acoustic Characterization of Contrast Agents for Medical Ultrasound Imaging*. Dordrecht: Kluwer Academic Publishers, 2001.

[17] C. E. Brennen, *Fundamentals of Multiphase Flow*. Cambridge University Press, 2005.

[18] H. Flanders, "Differentiation under the integral sign," *The American Mathematical Monthly*, vol. 80, no. 6, pp. 615–627, 1973.

[19] M. Emmer, *The onset of bubble vibration*. PhD thesis, Erasmus University Rotterdam, Jan. 2009.

[20] A. A. Doinikov and A. Bouakaz, "Review of shell models for contrast agent microbubbles," *IEEE Transactions on Ultrasonics, Ferroelectrics, and Frequency Control*, vol. 58, no. 5, pp. 981–993, 2011.

[21] L. Hoff, P. C. Sontum, and J. M. Hovem, "Oscillations of polymeric microbubbles: Effect of the encapsulating shell," *The Journal of the Acoustical Society of America*, vol. 107, no. 4, pp. 2272–2280, 2000.

[22] C. C. Church, "The effects of an elastic solid surface layer on the radial pulsations of gas bubbles," *The Journal of the Acoustical Society of America*, vol. 97, no. 3, pp. 1510–1521, 1995.

[23] C. Fang, *Incompressible Viscous Flows*, pp. 273–377. New York: Springer International Publishing, 2019.

[24] A. Qamar and R. Samtaney, "A model for an acoustically driven microbubble inside a rigid tube," *Journal of Fluids Engineering*, vol. 137, 02 2014.

[25] P. Zhong, Y. Zhou, and S. Zhu, "Dynamics of bubble oscillation in constrained media and mechanisms of vessel rupture in swl," *Ultrasound in Medicine and Biology*, vol. 27, pp. 119–134, Jan 2001.

[26] Y. Hu, S. Qin, T. Hu, K. W. Ferrara, and Q. Jiang, "Asymmetric oscillation of cavitation bubbles in a microvessel and its implications upon mechanisms of clinical vessel injury in shock-wave lithotripsy," *International Journal of Non-Linear Mechanics*, vol. 40, no. 2, pp. 341 – 350, 2005. Special Issue in Honour of C.O. Horgan.

[27] M. Ries. personal communication.

[28] G. Késmárky, P. Kenyeres, M. Rábai, and K. Tóth, "Plasma viscosity: A forgotten variable.," *Clinical Hemorheology Microcirculation*, vol. 39, no. 1-4, pp. 243 – 246, 2008.

[29] A. S. Popel and P. C. Johnson, "Microcirculation and hemorheology," *Annual Review of Fluid Mechanics*, vol. 37, pp. 43–69, Jan 2005.

[30] F. Lauwers, F. Cassot, V. Lauwers-Cances, P. Puwanarajah, and H. Duvernoy, "Morphometry of the human cerebral cortex microcirculation: General characteristics and space-related profiles," *NeuroImage*, vol. 39, no. 3, pp. 936 – 948, 2008.

[31] A. Løkkegaard, J. R. Nyengaard, and M. J. West, "Stereological estimates of number and length of capillaries in subdivisions of the human hippocampal region," *Hippocampus*, vol. 11, no. 6, pp. 726–740, 2001.

[32] H. Zheng, P. A. Dayton, C. Caskey, S. Zhao, S. Qin, and K. W. Ferrara, "Ultrasound-driven microbubble oscillation and translation within small phantom vessels," *Ultrasound Med. Biol.*, vol. 33, no. 12, pp. 1978–1987, 2007.

[33] H. N. Oguz and A. Prosperetti, "The natural frequency of oscillation of gas bubbles in tubes," *The Journal of the Acoustical Society of America*, vol. 103, no. 6, pp. 3301–3308, 1998.

[34] S. Qin and K. W. Ferrara, "The natural frequency of nonlinear oscillation of ultrasound contrast agents in microvessels," *Ultrasound in Medicine Biology*, vol. 33, no. 7, pp. 1140 – 1148, 2007.

A Fundamentals for fluid flows

Before reading the theory needed to understand the method used in this research, there is some terminology that needs to be addressed if one is not familiar with fluid dynamics. There are common used terms in physics with which a fluid can be described. These terms signify certain characteristic of the fluid. It is important to understand what those terms imply about the physics of the fluid. For this reason we will briefly go over a few of the definitions of these terms. Multiple physics books were consulted for this section [12][14][13].

Steady and unsteady flows

Depending on how a state changes in time, it can be described as either *steady* or *unsteady*. If fluid parameters (e.g. velocity, pressure, density etc.) are constant in time the fluid is said to be steady. If these parameters change with time the fluid is unsteady. Depending on the situation a fluid might be unsteady at first but develop into a steady fluid. One example of this is running water out of a tab. When the handle on the tab is turned to let the water out, the flow is unsteady. But after a while, when the tab is fully open, the flow becomes steady because no new changes are made within the system. The second part of this flow is also called a fully developed steady flow because all transient effects of opening the tab have vanished and it has settled into its final state.

Compressible and incompressible fluids

The terms *compressible* and *incompressible* are used to describe the density of a fluid. A fluid is considered incompressible if the density is constant. For a compressible fluid the fluctuations in the density are to large to be negligible and must be taken into account. Most liquids can be considered incompressible at moderate pressures because the density does not fluctuate much with change in temperature. For high pressures the compressible effects in the liquid become important and can't be neglected anymore. In the upcoming sections we will assume that the fluids are incompressible.

Viscous and inviscid fluids

In an *inviscid* fluid no viscous effects are taken into account because they can be neglected. Consequently, a *viscous* fluid is a fluid where these viscous effects can not be neglected. Thus, depending on the dynamics of your system, your fluid might be considered viscous of inviscid. Whether or not these effects can be neglected can be determined by computing the Reynolds number:

$$Re = \rho \frac{V\,L}{\mu} \tag{A.1}$$

with ρ the density, μ the viscosity of the fluid, V the characteristic velocity of your system and L the characteristic size scale of your system. For a large Reynolds number the viscous effect are negligible, and for small numbers they are not and dominate your system. For an intermediate Reynolds number it is unclear whether or not the viscous effect are negligible. This turning point is dependent on the geometry of the system.

Laminar and turbulent flows

The terms *laminar* and *turbulent* can be assigned to a viscous fluid to describe the behavior of the flow field. Laminar flow is when the fluid moves in smooth layers on top of each other. Take for example a laminar fluid flow in a circular pipe. Because we are dealing with a laminar flow, the fluid moves in layers in the direction of the fluid displacement, and thus has only a velocity component in this same direction. In turbulent flow the fluid particles in these layers can mix and thus there are velocity fluctuations in directions other than the displacement direction of the flow. This behavior creates more resistance to the flow which might be an unwanted phenomenon in some cases.
Turbulent flows are also more difficult to mathematically describe due to these rapid velocity fluctuations. Depending on the flow rate an flow is laminar or turbulent. Because of the complex nature of turbulent flows, we will assume that all flows in upcoming sections are laminar flows.

B 3-dimensional Navier-Stokes equations

The 3-dimensional Navier stokes equations in cartesian coordinates:

$$\rho\left[\frac{D\,u_x}{Dt}\right] = -\frac{\partial p}{\partial x} + \mu\nabla^2 u_x + f_x\,, \tag{B.1}$$

$$\rho\left[\frac{D\,u_y}{Dt}\right] = -\frac{\partial p}{\partial y} + \mu\nabla^2 u_y + f_y\,, \tag{B.2}$$

$$\rho\left[\frac{D\,u_z}{Dt}\right] = -\frac{\partial p}{\partial z} + \mu\nabla^2 u_z + f_z\,. \tag{B.3}$$

Here, ρ is the density of the fluid, μ the viscosity of the fluid and $u_r,\ u_\theta,\ u_z$ are the velocity components in the r, θ and z. In the equation above we have used the following operators:

$$\frac{D}{Dt} = \frac{\partial}{\partial t} + u_x\frac{\partial}{\partial x} + u_y\frac{\partial}{\partial y} + u_z\frac{\partial}{\partial z}\,, \tag{B.4}$$

$$\nabla^2 = \frac{\partial^2}{\partial x^2} + \frac{\partial^2}{\partial y^2} + \frac{\partial^2}{\partial z^2}. \tag{B.5}$$

The 3-dimensional Navier stokes equations in cylindrical coordinates:

$$\rho\left[\frac{D\,u_r}{Dt} - \frac{u_\theta^2}{r}\right] = -\frac{\partial p}{\partial r} + \mu\left[\nabla^2 u_r - \frac{u_r}{r^2} - \frac{2}{r^2}\frac{\partial u_\theta}{\partial\theta}\right] + f_r\,, \tag{B.6}$$

$$\rho\left[\frac{D\,u_\theta}{Dt}-\frac{u_\theta u_r}{r}\right]=-\frac{1}{r}\frac{\partial p}{\partial r}+\mu\left[\nabla^2 u_\theta-\frac{u_\theta}{r^2}-\frac{2}{r^2}\frac{\partial u_r}{\partial\theta}\right]+f_\theta\,, \tag{B.7}$$

$$\rho\left[\frac{D\,u_z}{Dt}\right]=-\frac{\partial p}{\partial z}+\mu\nabla^2 u_z+f_z\,. \tag{B.8}$$

Here, ρ is the density of the fluid, μ the viscosity of the fluid and $u_r,\ u_\theta,\ u_z$ are the velocity components in the r, θ and z. In the equation above we have used the following operators:

$$\frac{D}{Dt}=\frac{\partial}{\partial t}+u_r\frac{\partial}{\partial r}+\frac{u_\theta}{r}\frac{\partial}{\partial\theta}+u_z\frac{\partial}{\partial z}\,, \tag{B.9}$$

$$\nabla^2=\frac{\partial^2}{\partial r^2}+\frac{1}{r}\frac{\partial}{\partial r}+\frac{1}{r^2}\frac{\partial^2}{\partial\theta^2}+\frac{\partial^2}{\partial z^2}\,. \tag{B.10}$$

The 3-dimensional Navier stokes equations in spherical coordinates:

$$\begin{gathered}\rho\left[\frac{D\,u_r}{Dt}-\frac{u_\theta^2+u_\phi^2}{r}\right]=\\ -\frac{\partial p}{\partial r}+\mu\left[\nabla^2 u_r-\frac{2u_r}{r^2}-\frac{2}{r^2}\frac{\partial u_\theta}{\partial\theta}-\frac{2u_\theta\cot\theta}{r^2}-\frac{2}{r^2\sin\theta}\frac{\partial u_\phi}{\partial\phi}\right]+f_r\,,\end{gathered} \tag{B.11}$$

$$\begin{gathered}\rho\left[\frac{D\,u_\theta}{Dt}+\frac{u_r u_\theta}{r}-\frac{u_\theta u_\phi\cot\theta}{r}\right]=\\ -\frac{1}{r}\frac{\partial p}{\partial\theta}+\mu\left[\nabla^2 u_\theta+\frac{2}{r^2}\frac{\partial u_r}{\partial\theta}-\frac{u_\theta}{r^2\sin^2\theta}-\frac{2\cot\theta}{r^2\sin\theta}\frac{\partial u_\phi}{\partial\phi}\right]+f_\theta\,,\end{gathered} \tag{B.12}$$

$$\begin{gathered}\rho\left[\frac{D\,u_\phi}{Dt}+\frac{u_\phi u_r}{r}+\frac{u_\theta u_\phi\cot\theta}{r}\right]=\\ -\frac{1}{r\sin\theta}\frac{\partial p}{\partial\theta}+\left[\nabla^2 u_\phi+\frac{2}{r^2 sin\theta}\frac{\partial u_r}{\partial\phi}-\frac{u_\phi}{r^2\sin^2\theta}+\frac{2\cot\theta}{r^2\sin\theta}\frac{\partial u_\theta}{\partial\phi}\right]+f_\phi\,.\end{gathered} \tag{B.13}$$

Here, ρ is the density of the fluid, μ the viscosity of the fluid and u_r, u_θ, u_z are the velocity components in the r, θ and z. In the equation above we have used the following operators:

$$\frac{D}{Dt} = \frac{\partial}{\partial t} + u_r \frac{\partial}{\partial r} + \frac{u_\theta}{r} \frac{\partial}{\partial \theta} + \frac{u_\phi}{r \sin\theta} \frac{\partial}{\partial \phi}, \tag{B.14}$$

$$\nabla^2 = \frac{1}{r^2} \frac{\partial}{\partial r} \left(r^2 \frac{\partial}{\partial r} \right) + \frac{1}{r^2 \sin\theta} \frac{\partial}{\partial \theta} \left(\sin\theta \frac{\partial}{\partial \theta} \right) + \frac{1}{r^2 \sin^2\theta} \frac{\partial^2}{\partial \phi^2} \,. \tag{B.15}$$